POLITECNICO DI TORINO

Master's Degree in Energy and Nuclear Engineering

Master's Degree Thesis

Performance evaluation of high-efficiency cyclones

Supervisors

Prof. Paolo Maria TRONVILLE

Candidate

Rafael VENANCIO DURAND

MARCH 2025

Abstract

This study evaluates the performance of two high-efficiency cyclones – the Stairmand HE and Swift HE designs – for application in an inertial separator for condensable substances, a system aimed at recovering volatile organic compounds from industrial exhaust gases. The cyclones were designed to operate at 8 m^3/h, manufactured via selective laser sintering using polyamide PA2200, and experimentally tested in an aerosol test rig using DEHS to measure fractional collection efficiency and pressure drop across flow rates of 3, 4.5, 6, 8, and 10 m^3/h. Experimental results were compared with predictions from the Iozia and Leith theoretical model. The Stairmand HE cyclone showed strong agreement with the model at 4.5, 6, and 8 Sm^3/h, with mean absolute errors ranging from 3.42% to 6.15% and overlap coefficients of approximately 90%, whereas the Swift HE cyclone consistently exhibited higher experimental efficiencies than predicted, particularly at elevated flow rates, indicating limitations of the model for this geometry. Increasing the flow rate improved collection efficiency and reduced cut diameter, but also increased pressure drop. Overall, the Stairmand HE cyclone demonstrated a closer match to theoretical predictions, making it a more reliable option for applications requiring accurate performance forecasting, while future validation should involve testing both cyclones directly in the real ISCS operating environment.

Keywords: Cyclone separator. High-efficiency cyclone. Collection efficiency. Pressure drop. Aerosol. Particle separation. Inertial separator.

Table of Contents

List of Tables

List of Figures

Chapter 1

Introduction

Char, sometimes used as a synonym of natural pyrogenic organic matter (PyOM), is a material produced by the incomplete combustion of organic matter, whether from natural processes or human activities. This process is known as pyrolysis of biomass (in most of the cases, wood). Pyrolysis is the thermal decomposition of a solid fuel in an oxygen-free, inert atmosphere, producing a liquid or gaseous fuel and a solid byproduct (char). Depending on its application, PyOM may be referred to as activated carbon, biochar, charcoal, among other names [1, 2].

Activated carbon refers to any form of carbon capable of adsorption. In addition to its adsorptive properties, activated carbon can also function as a catalyst and is used as an electrode in microbial fuel cells. Today, the growing global demand for activated carbon is driven by several markets, including drinking water treatment, energy storage technologies, and environmental applications influenced by new regulations. Biochar, on the other hand, is a carbon-rich material characterized by its high carbon content, fine-grained structure, and porous nature. In agriculture, it is used in various ways: to enhance soil fertility, improve nutrient absorption, and increase water retention. It also benefits soil microbial communities by providing habitats for microbial populations. Furthermore, in civil engineering, biochar has been investigated as a substitute for cement due to its positive effects on the compressive and tensile strength of concrete [1, 3].

When char is used as a fuel or as an industrial reducing agent, it is classified as charcoal. Brazil is the global leader in charcoal production; between 2019 and 2022, production increased by 18.5%, reaching 24.2 million cubic meters in 2023. Charcoal is primarily used in the steel industry, where it serves as a reducing agent, offering higher purity than coal, along with low sulfur and ash content. In Brazil, approximately 65% of charcoal production is carried out by small and medium-sized producers. The production sites, known as charcoal kiln sites, are typically located near the wood sources used for charcoal production. The activities carried out in a charcoal plant are summarized in Table 1.1 [1, 4, 5, 6].

Activity	Description
Cutting	Tree cutting and stump removal are done using chainsaws, tractors, or manual tools like sickles and axes
Stacking and bundling	Branches are removed to help arrange logs in the kiln, then the wood is dried for 15 to 30 days before being bundled
Transport	Firewood is transported to the kilns using animals or tractors, based on the plant's scale
Loading	The kiln interior is cleaned of leftover charcoal, the floor is lined with dry leaves to retain heat, and firewood is manually loaded and arranged inside the kiln to maximize space and efficiency
Closing and sealing	The kiln opening is sealed with bricks and a paste made from local rock ("tauá") and water to ensure airtight closure
Carbonization	The kiln is lit through an upper opening and the carbonization process, lasting around three days, is carefully monitored by controlling airflow via specific vents
Sealing	At the end of carbonization, the kiln is sealed with tauá to block air and prevent charcoal combustion, followed by cooling of the kiln
Opening, unloading and transfer	Charcoal is removed from the kiln with a pitchfork, placed into containers, transported to a designated area, and left to cool on the ground
Bagging and loading	Charcoal is packed into bags and loaded onto bulk transport trucks

Table 1.1: Activities developed in a charcoal kiln site [6]

The process that occurs inside the masonry oven is known as slow pyrolysis, also referred to as carbonization in some sources. This technique involves a maximum temperature range of 400 to 650 °C, with a minimum heating rate between 5 and 7 °C/min, a maximum heating rate between 20 and 100 °C/min, and a residence

time ranging from 5 to 30 minutes up to several days. This combination allows for a higher yield of high-quality char while minimizing the production of liquid and gaseous byproducts [7]. According to Santos and Hatakeyama [8], the steps involved in charcoal's carbonization are:

1. Drying: occurs up to 110 °C, during which only moisture is released;

2. Torrefaction: takes place between 110 and 250 °C. At around 180 °C, the release of bound water begins due to the decomposition of cellulose and hemicellulose. There is little weight loss up to 250 °C. At this stage, char or torrefied wood is formed;

3. Carbonization: occurs between 250 and 350 °C. As the decomposition of cellulose and hemicellulose intensifies, significant weight loss occurs, forming gas, oil, and water. Upon reaching 350 °C, the charcoal contains about 75% fixed carbon, and carbonization is considered nearly complete;

4. Fixation: from 350 °C onward, there is a gradual reduction in the release of volatile elements, mainly combustible gases, while carbon fixation continues.

Traditional charcoal plants typically consist of batches of 12 or 18 kilns (Figure 1.1), which are generally of three main types: hillside kilns, "hot-tail" kilns, and surface kilns (Figure 1.2). Operations are carried out in cycles; for example, in a charcoal plant with 18 kilns arranged in two rows, each row is managed by two charcoal workers. While three kilns are being loaded, three are in the carbonization phase, and three are cooling down, ensuring continuous operation [6].

(a) Firewood branches **(b)** Batch of kilns

Figure 1.1: Views of a charcoal production plant in Cabrália Paulista, Brazil

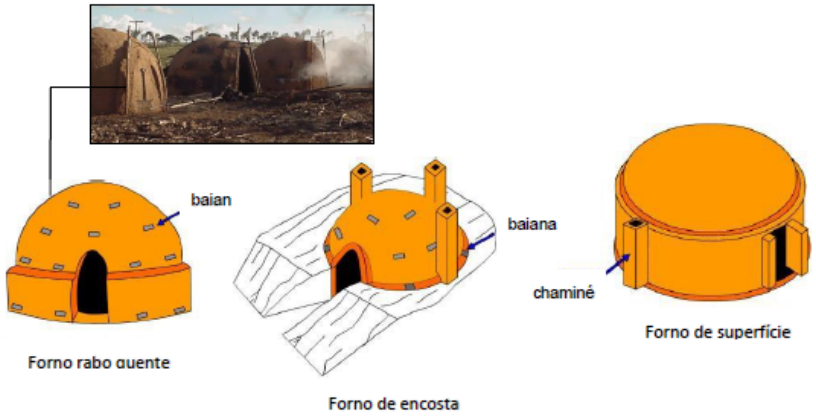

Figure 1.2: Types of kilns used for charcoal production [6]

The future of charcoal production is closely tied to trends in the steel industry. According to the World Steel Association, in 2023, the carbon dioxide (CO_2) emissions intensity of steel production was estimated at 1.92 t CO_2/t of steel. For comparison, according to the International Energy Agency (IEA), the CO_2 emissions intensity of the cement industry in the same year was estimated at 0.6 t CO_2/t of cement (3.2 times lower). As a result, decarbonizing the steel industry has become a major challenge. In response, "green steel" — steel produced using low-CO_2-emission methods — has emerged as a key trend [4, 9, 10, 11].

In this context, companies that adopt environmentally friendly practices can position themselves as preferred suppliers to steelmakers committed to reducing their carbon footprint. Several actions to promote sustainable charcoal production have been undertaken, including research and development of cleaner technologies, the promotion of forest management, and the enforcement of measures against illegal deforestation. Furthermore, initiatives such as replacing traditional ovens with more efficient production systems and recovering byproducts from the pyrolysis process — such as the utilization of charcoal fines — also reflect an industrial shift toward more sustainable practices [4].

During the pyrolysis process, in addition to char, bio-oil and tars are also produced. Bio-oil is a liquid fuel that can be easily stored and efficiently transported, enabling decentralized use in turbines, engines, or boilers. On the other hand, tars, which are condensable volatile organic compounds (VOCs — primarily alkanes, alkenes, aromatic hydrocarbons, and oxygenated compounds), are classified as hazardous air pollutants (HAPs). HAPs are airborne compounds that pose significant risks to human health and the environment, as they can cause cancer, birth defects, and other serious health problems. Consequently, they represent a safety risk for workers exposed to them, making their strict regulation essential [2, 12, 13, 14].

There are several technologies available for treating waste gases with high concentrations of VOCs, such as catalytic oxidation and electrostatic precipitation. However, these methods are only feasible when the fumes contain particles, that is, condensed vapors, and the separators used require extensive maintenance, as the filters must be disassembled and transported to specialized cleaning facilities for regeneration. Furthermore, the aforementioned cleaning technologies overlook the potential to further exploit certain substances, such as bio-oil, as value-added products for sale [14].

1.1 Motivation

The inertial separator for condensable substances (ISCS) serves a dual purpose: it purifies exhaust fumes while simultaneously recovering pollutants. Separation is achieved by promoting the condensation of gaseous contaminants, particularly those with low vapor pressure. This innovative technology effectively reduces emissions by removing, in many cases, toxic and carcinogenic substances from the airstream before it is released into the atmosphere [14].

The applications of the ISCS are not limited to charcoal production. In fact, it can be applied to any industrial process that emits VOCs. For example, in the rubber industry, vulcanization—a chemical process used to enhance the elasticity and strength of rubber—results in significant VOC emissions. Similarly, in the coffee roasting process, where beans are heated to temperatures above 200 °C to develop their characteristic flavor and aroma, over 1,000 volatile compounds are produced, with around 30 primarily responsible for the aroma. These valuable compounds are typically lost as byproducts, but with the ISCS, they can be recovered and potentially commercialized [14].

Figure 1.3 shows a schematic of the ISCS. Hot fumes from the industrial process are immediately mixed with a cold flow. This mixing brings the volatile contaminants to saturation, triggering their condensation. The cold flow is introduced using a “nucleator”, which is designed to provide sufficient time and space for the nucleation, growth, and coagulation of liquid contaminant particles. Downstream of this localized condensation, an inertial separator removes the liquid particles from the gas stream, resulting in cleaner exhaust. A portion of the cleaned gas is sent to a refrigeration unit, where it is cooled to a temperature that promotes further condensation of volatile substances, while the remaining gas is recirculated back to the furnace to complete the loop. A first prototype was built using a high-efficiency cyclone — an inertial separator (Figure 1.4) — designed to operate at a flow rate of 10 m^3/h with a collection efficiency of 50% for particles measuring 1.44 μm [14].

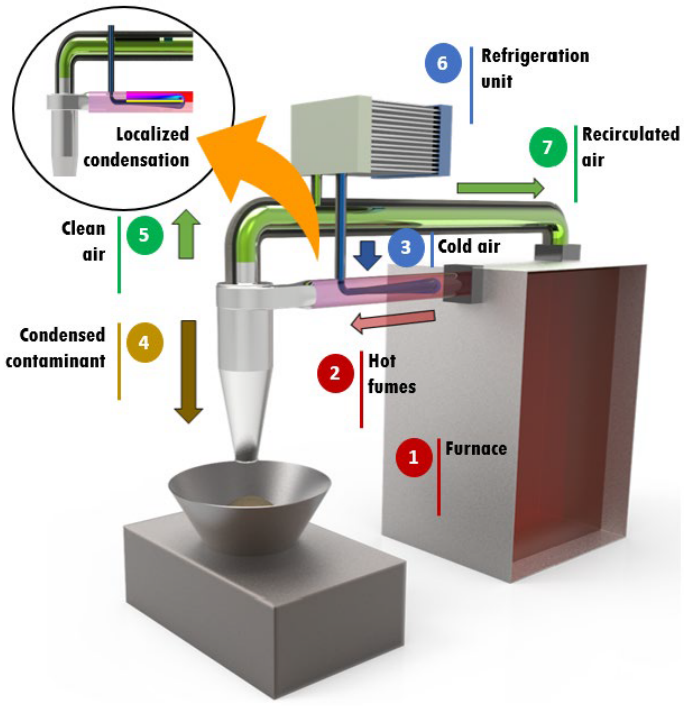

Figure 1.3: Representation of main parts of the ISCS [14]

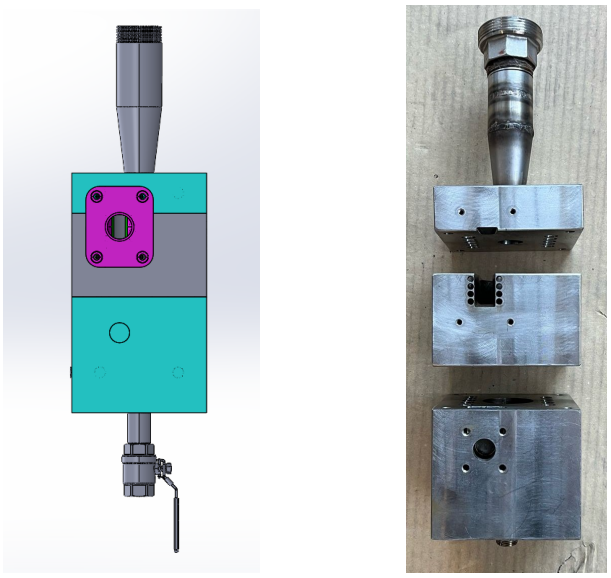

(a) Drawing **(b)** Manufactured

Figure 1.4: Previous cyclone

The prototype's performance was evaluated using dipropylene glycol — commonly employed in the medical field as an antifreeze — as the organic substance subjected to boiling. A mixture of dry ice (solid CO_2 at –80 °C), salt, and water was used as the refrigerant fluid responsible for cooling the cold stream. Two tests were conducted under distinct operating conditions, with emphasis on the temperature of the refrigerant fluid. In the first test, a mixture containing 30% dry ice was employed, resulting in a temperature of 0.5 °C. In the second test, the dry ice content was increased to 70%, yielding a temperature of approximately –9.5 °C. The collection efficiency and thermal power obtained in each test are presented in Figure 1.5 [14].

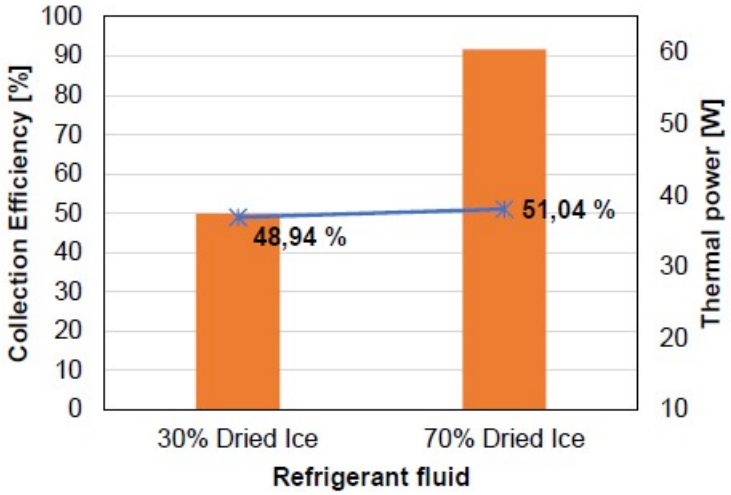

Figure 1.5: Collection efficiency and thermal power during each test [14]

The results presented in Figure 1.5 indicate that achieving a modest improvement in collection efficiency required nearly doubling the thermal power supplied to the system. This finding highlights the need to understand both the behavior of the contaminants generated and their saturation limits, in order to design a refrigeration strategy that minimizes energy consumption [14]. On the other hand, the results also suggest that the inertial separator may not be operating as intended, reinforcing the need for a more detailed assessment of its performance and the potential development of an improved design.

1.2 Scope

The objective of this study is to develop a new cyclone separator designed to meet the operational requirements of the ISCS system (Figure 1.6). Achieving this goal

demands a comprehensive understanding of the fluid-dynamic behavior, collection efficiency, and energy consumption associated with different high-performance cyclone geometries.

Figure 1.6: Cyclone separator for the ISCS

To this end, two high-efficiency cyclone designs were selected, constructed, and subjected to controlled experimental testing. Their aerodynamic performance was assessed through detailed measurements of fractional collection efficiency and pressure drop over a range of operational conditions. These experimental results were then compared with a specific theoretical model available in the literature, enabling a critical evaluation of how accurately it captures the behavior of this type of particle collector.

1.3 Organization

This document is organized into five chapters, each addressing a specific stage of the study and collectively guiding the reader from the theoretical foundations

to the final conclusions. Chapter 2 introduces the theoretical aspects relevant to particle collection systems, with particular emphasis on cyclone separators. It reviews the fundamental principles regarding working principle, sizing, collection efficiency and pressure drop. Additionally, this chapter presents the mathematical formulations and validation methods commonly used to assess the accuracy of theoretical and semi-empirical models in predicting cyclone performance. These discussions provide the necessary background for interpreting the experimental results presented later in the work.

Chapter 3 describes in detail the methodological development of the project. It outlines the complete design procedure adopted for the two high-efficiency cyclones, including geometric dimensioning and fabrication procedure. The chapter also presents the arrangement of the experimental setup, instrumentation, measurement procedures, and the protocol used to evaluate fractional efficiency and pressure drop.

Chapter 4 reports the results obtained from the experimental campaign. The data are presented in a structured manner, accompanied by the corresponding theoretical predictions for comparison. The chapter discusses key trends, discrepancies, and performance indicators, providing a critical interpretation of the behavior of both cyclone configurations.

Finally, Chapter 5 concludes the work by summarizing the main findings and their implications for the design of a new cyclone for the ISCS system. The chapter also highlights the limitations of the study and suggests opportunities for future research and optimization efforts.

Chapter 2

Literature Review

This chapter presents the main topics related to particle collectors, with a particular focus on cyclones. Moreover, some methods for model validation are depicted.

2.1 Particle Collectors

Particle collectors are devices responsible for the separation and collection of particles from a gas stream. The operation of these instruments is usually based on one or more combined particle separation mechanisms, which are generally classified as gravity settlement, inertial deposition or inertial impaction, flow-line or direct interception, diffusional deposition, electrostatic deposition, thermal precipitation and agglomeration [15].

The most famous particle collectors are: gravity settling chambers, impingement separators, cyclone separators, electrostatic precipitators (ESPs), fabric filters, and wet scrubbers. The selection of this kind of device is not always an easy task due to various impact factors, such as the concentration and particle size distribution, the level of purification required, the gas and particle properties (for example, density, viscosity, solubility, flammability, chemical and biological aggressiveness), ease of cleaning and maintenance, and costs (manufacturing, operation, and maintenance) [15, 16, 17].

Table 2.1 shows the performance of some of these devices. Cyclones are simple to manufacture and operate, can undergo high-temperature conditions and present low cost; however, they present low collection efficiency values for small particles and are sensitive to variable dust loading and flow rate. Wet scrubbers promote gas absorption and particle removal simultaneously, but suffer from corrosion and erosion. In addition, to avoid contamination of the effluent stream by liquid entrainment, a wastewater treatment unit must be added, increasing the costs. ESPs can obtain high value for collection efficiency, can collect very small particles,

and, as the cyclones, can operate at high temperatures, even so they have a relatively high investment cost and are sensitive to variable dust loadings, flow rates or resistivity. Finally, fabric filters can achieve the highest collection efficiency values and collect the smallest possible particles; nevertheless, they are expensive devices and cannot operate at high temperatures or high relative humidity [15, 18].

Device	**Minimum particle size [μm]**	**Collection efficiency [%]**
Cyclone	5-25	50-90
Wet scrubber	>0.5-10	<80
ESP	<1	95-99
Fabric filter	<1	>99

Table 2.1: Performance of some separation devices [15]

2.1.1 Mass Balance

Consider the "black-box model" for a generic particle collector shown in Figure 2.1.

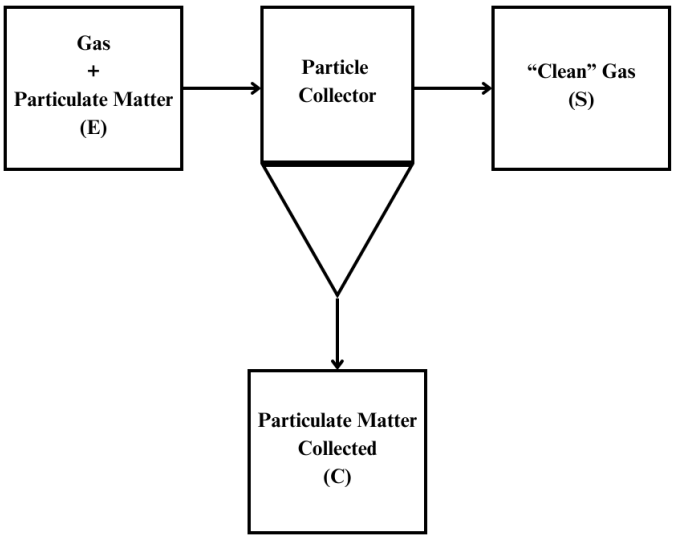

Figure 2.1: Schematic of a generic particle collector [18]

Under the hypothesis of steady-state condition, the mass balance for the gas stream imposes that the mass flow rate at the inlet of the particle collector ($\dot{m}_E$) should be equal to the outlet ($\dot{m}_S$) (Equation 2.1) [18].

$$\dot{m}_E = \dot{m}_S \tag{2.1}$$

Furthermore, the gas mass flow rate is equal to the product of density (ρ) and volumetric flow rate (Q) [18]. Thus:

$$\rho_E Q_E = \rho_S Q_S \tag{2.2}$$

Assuming the hypothesis of ideal gas, the density is given by Equation 2.3 [18].

$$\rho = \frac{PM}{RT} \tag{2.3}$$

Where P and T are the pressure and temperature of the stream, respectively, M is the molecular weight of the gas, and R is the universal gas constant ($R = 8.3145\, J \cdot mol^{-1} \cdot K^{-1}$). Thus, Equation 2.4 shows the relation between the inlet and outlet volumetric flow rate [18].

$$Q_S = Q_E \left(\frac{T_S}{T_E}\right) \left(\frac{P_E}{P_S}\right) \tag{2.4}$$

Assuming that both temperature and pressure variations in the particle collector are negligible, the volumetric flow rate remains constant (Equation 2.5) [18].

$$Q_S = Q_E = Q \tag{2.5}$$

With respect to particles, the mass balance imposes that the mass flow rate at the inlet of the particle collector (W_E) is equal to the sum of the mass flow rate at the outlet (W_S) and the mass flow rate collected (W_C) (Equation 2.6) [18].

$$W_E = W_S + W_C \tag{2.6}$$

Moreover, the particle mass flow rate is equal to the product of the mass concentration (C) and the volumetric flow rate [18].

2.1.2 Global and Fractional Collection Efficiencies

The collection efficiency measures the performance of a particle collector. In this sense, two different efficiencies can be defined: global and fractional. The global efficiency (η) is shown in Equation 2.7 [17, 18].

$$\eta = \frac{W_C}{W_E} = \frac{W_E - W_S}{W_E} \tag{2.7}$$

If both temperature and pressure do not change during the process ($Q_E = Q_S$), Equation 2.8 can be used instead [17, 18].

$$\eta = \frac{C_E - C_S}{C_E} \tag{2.8}$$

However, most aerosols are polydisperse, that is, they are composed of particles with different sizes that can range over two or more orders of magnitude. Furthermore, each particle collector has a different behavior for different particle sizes. Thus, it is also important to define an efficiency that is a function of the diameter of the particle (d_p) - the fractional efficiency (η_i) (Equation 2.9) [17, 18, 19].

$$\eta_i = \frac{W_{E,i} - W_{S,i}}{W_{E,i}} \tag{2.9}$$

Where $W_{E,i}$ and $W_{S,i}$ are the mass flow rate for a certain particle range i at the inlet and at the outlet of the particle collector, respectively [17, 18].

2.2 Cyclone Separators

Cyclone separators are devices that use an inertial impaction mechanism, created by a rotating gas flow, to separate particles from the gas. In addition to their simple design, ease of operation, and low cost, they are very compact in most applications and highly robust. However, they can suffer from erosive wear and fouling — particularly when processing abrasive or "sticky" particles — and may operate below expectations if not properly designed or operated [15, 20].

Cyclones are among the most widely used particle collectors for gas-solid separation. Modern applications include the oil and gas industry, power generation plants, the iron and steel industry, cement plants, coal-fired boilers, and more. Since their efficiency is very high for large particles (d_p>10 μm), they are often used as precollectors installed upstream of ESPs or fabric filters, which are more effective at capturing smaller particles. Moreover, these devices can handle a wide range of gas flow rates — from 50 to 50,000 m^3/h. However, when the total flow rate exceeds 20,000 m^3/h, it is common practice to divide the flow among multiple parallel cyclones to avoid scaling issues with blowers and other equipment. Additionally, smaller cyclones tend to be more efficient [20, 21].

There are three types of conventional cyclones: reverse-flow cyclones (with tangential or axial inlets), straight-through-flow cyclones, and impeller collectors. In practice, tangential-inlet reverse-flow cyclones are by far the most common configuration. Axial-inlet reverse-flow cyclones, which are equipped with swirl vanes and have a cylindrical body, are also known as swirl tubes [15, 20].

2.2.1 Operating Principle

Inertial impaction refers to the transfer of particles onto surfaces due to their inertia and is the most extensively studied particle separation mechanism, both theoretically and experimentally, in the literature. When a gas flows around

an obstacle, two extreme behaviors can be observed: very small particles with negligible inertia follow the gas streamlines closely, while large, heavy particles tend to continue moving in a straight line — largely unaffected by changes in the gas flow — and may impact the surface of the obstacle (Figure 2.2) [19].

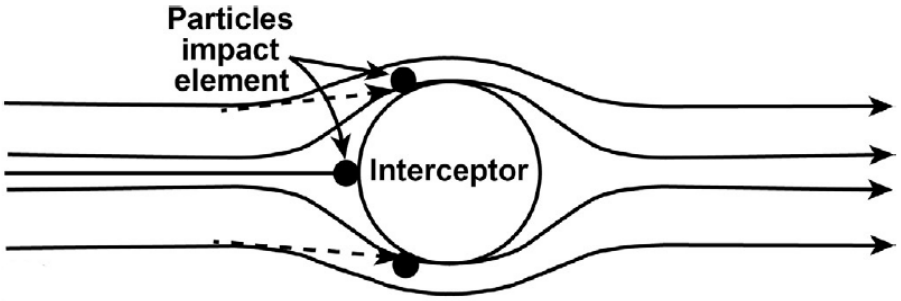

Figure 2.2: Inertial impaction mechanism [15]

Inertial impaction is governed by a dimensionless parameter referred to as the Stokes number (Stk). This parameter is defined as the ratio of the particle stopping distance (d_s) to a characteristic dimension of the obstacle, typically the vortex finder diameter (D_e) in the case of a cyclone. The stopping distance represents the length over which a particle decelerates to rest due to the drag force exerted by the surrounding fluid. It can be expressed by means of Equation 2.10 [19, 20].

$$d_s = U_0 \tau \tag{2.10}$$

Where U_0 is the undisturbed gas velocity well away from the obstacle, and τ is the particle relaxation time, which can be expressed by Equation 2.11 [19].

$$\tau = \frac{\rho_p d_p^2}{18\mu} \tag{2.11}$$

Where ρ_p is the particle density and μ is the dynamic (absolute) viscosity of the gas. By substituting Equations 2.10 and 2.11 into the definition of the Stokes number, the final expression for Stk is obtained (Equation 2.12) [19].

$$Stk = \frac{d_s}{D_e} = \frac{\rho_p d_p^2 U_0}{18\mu D_e} \tag{2.12}$$

For large Stokes numbers ($Stk >> 1$), particles exhibit a strong tendency to maintain their trajectory when the gas flow changes direction. Conversely, for very small Stokes numbers ($Stk << 1$), particles closely adhere to the gas streamlines [19].

Inertial impaction is the physical mechanism behind the operation of a cyclone. When the gas flow enters the device, it is directed along its curved shape, creating a helical flow pattern inside the equipment. Although small particles will follow the curved streamlines, large particles will continue to move in a straight line. These larger particles eventually collide with the outer wall and fall as a result of gravity. The particles then slide down the walls to the storage container. At the bottom of the cyclone, the clean gas flow reverses, forming a smaller inner core that exits at the top of the unit. A vortex finder tube, which extends downward in the cylinder, helps guide the inner vortex out of the device. Figure 2.3 shows the operation of a tangential-inlet reverse-flow cyclone [15, 19, 21].

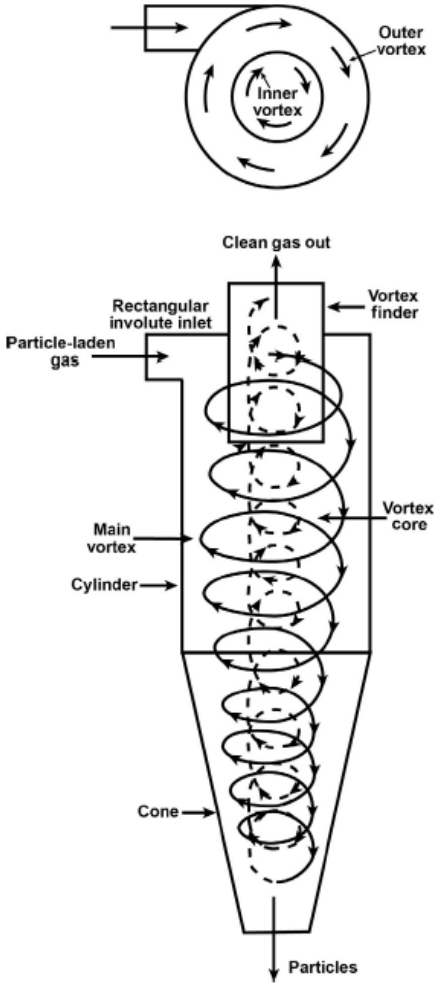

Figure 2.3: Reverse-flow cyclone with tangential inlet [15]

2.2.2 Sizing

In addition to the diameter of the vortex finder, the geometry of a reverse-flow cyclone with tangential inlet can be fully described by other seven dimensions: diameter of the cylindrical body (D), height of inlet (a), width of inlet (b), total height (H), height of the cylindrical body (h), particle outlet diameter (B), and vortex finder (or gas exit) length (S). Figure 2.4 shows each of these dimensions in the device [20, 21].

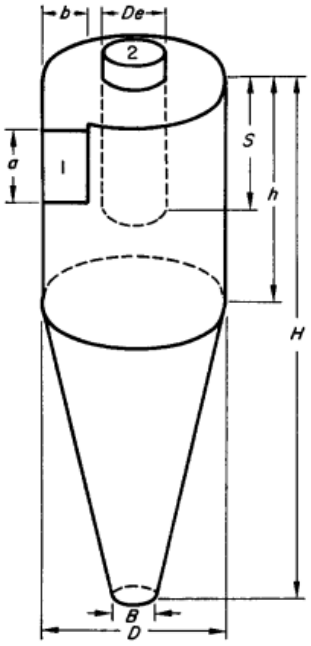

Figure 2.4: Relevant dimensions of a reverse-flow cyclone with tangential inlet [22]

Normally, the relevant dimensions of a cyclone are given as a multiple of the diameter of the cylindrical body (geometric ratio). This allows a comparison of the geometric similarity of several cyclones without introducing absolute magnitudes. To estimate these dimensions, first D is calculated using Equation 2.13, where R is a recommended ratio, and then all other dimensions are obtained by multiplying the calculated value by the corresponding geometric ratio. Furthermore, there are at least six standard cyclones available in the literature, each with a fixed value for each ratio (Table 2.2) [21, 22].

$$D = \sqrt{\frac{Q}{R}} \tag{2.13}$$

Ratio	Lapple GP	Swift GP	Stairmand HE	Swift HE	Stairmand HT	Swift HT	Unit
R	6860	6680	5500	4940	16500	12500	m/h
a/D	0.500	0.500	0.500	0.440	0.750	0.800	-
b/D	0.250	0.250	0.200	0.210	0.375	0.350	-
H/D	4.000	3.750	4.000	3.900	4.000	3.700	-
h/D	2.000	1.750	1.500	1.400	1.500	1.700	-
D_e/D	0.500	0.500	0.500	0.400	0.750	0.750	-
B/D	0.250	0.400	0.375	0.400	0.375	0.400	-
S/D	0.625	0.600	0.500	0.500	0.875	0.850	-

Table 2.2: Recommended and geometric ratios for some standard cyclones [21, 22]

In Table 2.2, GP, HE and HT stand for general purpose, high efficiency, and high throughput, respectively. For a given value of Q, general-purpose and high-efficiency cyclones tend to have larger dimensions for the cylindrical body (both diameter and height) and the total height than high-throughput cyclones, while both gas inlet and outlet are approximately equal for all of them. Moreover, the vortex finder length is always greater than or equal to the inlet height to prevent the gas from short-circuiting the cyclone by bypassing directly from the inlet to the outlet without creating a vortex; the width of inlet is less than or equal to the difference between the radius of the cylindrical body and the radius of the vortex finder to avoid excessive pressure drop; the total height is at least three times greater than the diameter of the cylindrical body to maintain the vortex end within the conical section of the cyclone; for high-efficiency cyclones, the values of D_e/D, H/D_e and S/D_e are approximately in the range of 0.4-0.5, 8-10 and 1, respectively, to ensure maximum efficiency; and the inclination angle of the conical section must be between 7° and 8° to ensure fast dust sliding. Hence, the design of this type of device involves a compromise between collection efficiency, pressure drop, and size. Higher efficiencies typically result in greater pressure drops and larger unit sizes [15, 22, 23].

2.2.3 Collection Efficiency

The collection efficiency is a measure of the performance of a cyclone. One of the parameters that most impact the efficiency of this kind of device is the inlet gas velocity. An increased inlet velocity implies an increased particle stopping distance, and, consequently, a higher Stokes number. Thus, as velocity increases, more particles will not follow the streamlines and will collide with the internal wall of the cyclone, improving the efficiency of the equipment. Other parameters such as particle size, diameter and length of the cyclone's body, diameter of the vortex

finder, gas inlet area, and number of gas revolutions also affect device performance [15, 19].

Today, numerical simulation tools, such as computational fluid dynamics (CFD), are often used to evaluate the performance of new cyclone configurations. Determining the motion of particles inside a cyclone is a difficult fluid mechanics problem. First, the flow field is defined, that is, the pattern of streamlines for the gas flow inside the device. Since cyclones have a complex geometry, this step can only be done by using CFD. Once the flow field is defined, the actual trajectory of the particles can be computed relative to that of the gas [19]. For example, Yang et al. [24] investigated the separation performance of a cyclone separator after reshaping its cylindrical body by installing triangular helical fins. A numerical simulation using Ansys Fluent software was performed to optimize the structure of the cyclone. The results showed that the tangential velocity increased with the helical triangular fins and so the collection efficiency. Sylvia et al. [25] studied a cyclone for fine particle separation ($PM_{2.5}$) in palm oil mills. More specifically, a cyclone with a filter on the vortex finder was designed, and its performance was evaluated in terms of collection efficiency and pressure drop using CFD. As a result, the $PM_{2.5}$ removal efficiency reached 98% while the decrease in pressure was only 93 Pa higher than that of conventional devices.

Alternatively, several mathematical methods have been developed to predict the fractional efficiency of a cyclone. The reason for many different results derives from the different assumptions and simplifications taken with respect to the gas flow pattern and the motion of the particles through the cyclone. Some of them are: Lapple (1950), Barth (1956), Sproull (1970), Leith and Litch (1972), Dietz (1981), Mothes and Löffler (1988), Iozia and Leith (1990) [20, 21, 22, 26]. However, Leith and Mehta [22], based on a limited comparison between literature data and theoretical calculations, concluded that the Leith and Litch method appears to be more accurate than the methods of Lapple, Barth and Sproull. Furthermore, Dirgo and Leith [27] measured the collection efficiency of a Stairmand HE cyclone and judged that the Lapple, Leith-Litch, and Dietz models did not accurately predict the experimental results obtained.

Unlike the others, the Iozia and Leith theory is based on a mathematical and physical method known as regression analysis based on dimensional analysis (RABDA). It distinguishes itself from other theoretical models since it does not require an in-depth understanding of the mechanisms and processes involved in gas-particle flow and separation. RABDA correlates the separation parameter with the geometrical and operating condition parameters of a cyclone on the basis of the results of the dimensional analysis. The model coefficients are determined using multiple linear or non-linear regression techniques. This model, developed from a static particle approach and based on the results of 26 experiments carried out under ambient conditions, can describe the relationship between collection efficiency

and particle size reasonably well. The model states that the fractional collection efficiency of a cyclone can be described using a logistic function (Equation 2.14) [21, 26, 28, 29].

$$\eta_i = \frac{1}{1 + \left(\frac{d_{50}}{d_i}\right)^{\beta}} \tag{2.14}$$

Where d_i is the Stokes diameter of the particle whose collection efficiency is η_i, d_{50} is the Stokes cut diameter, that is, the diameter of the particle with 50% of collection efficiency, and β is an exponent that depends on d_{50} and the geometry of the cyclone. The value of d_{50} can be estimated using Equation 2.15 [21, 28].

$$d_{50} = \sqrt{\frac{9\mu Q}{\pi \rho_p Z_c v_{t,max}^2}} \tag{2.15}$$

Where ρ_p is the density of the particle, Z_c is the natural length of the cyclone, and $v_{t,max}$ is the maximum tangential gas velocity. The natural length is a function of the diameter of the central axis d_c (Equation 2.16) [15, 21, 28].

$$d_c = 0.47D \left(\frac{ab}{D^2}\right)^{-0.25} \left(\frac{D_e}{D}\right)^{1.4} \tag{2.16}$$

Knowing the value of d_c, it is possible to estimate the value of Z_c using Equation 2.17 [21, 28].

$$Z_c = \begin{cases} H - S,\ d_c \leq B \\ H - S - \left[\frac{H-h}{(D/B)-1}\right]\left[\left(\frac{d_c}{B}\right) - 1\right],\ d_c > B \end{cases} \tag{2.17}$$

Moreover, the maximum tangential gas velocity is a function of the cyclone geometry (Equation 2.18) [21, 28].

$$v_{t,max} = 6.1v \left(\frac{ab}{D^2}\right)^{0.61} \left(\frac{D_e}{D}\right)^{-0.74} \left(\frac{H}{D}\right)^{-0.33} \tag{2.18}$$

Where v is the gas velocity at the inlet of the cyclone (Equation 2.19) [21].

$$v_{=}\frac{Q}{ab} \tag{2.19}$$

A correlation for the exponent β was derived from 11 experiments performed under ambient conditions (Equation 2.20) [21, 29].

$$\ln \beta = 0.62 - 0.87 \ln\left(\frac{d_{50}}{10^4}\right) + 5.21 \ln\left(\frac{ab}{D^2}\right) + 1.05 \left[\ln\left(\frac{ab}{D^2}\right)\right]^2 \tag{2.20}$$

In Equation 2.20, d_{50} is given in micrometers. Figure 2.5 shows the fractional efficiency curves for the six standard cyclones in Table 2.2 for an aerosol with ρ_p=900 kg/m^3 operating at Q=10,000 m^3/h and normal conditions (0 °C and 1 atm). High-throughput cyclones exhibit a sharper cut (i.e., a steeper slope in the fractional efficiency curve) compared to general-purpose and high-efficiency cyclones. However, high-efficiency cyclones typically have a lower cut diameter than high-throughput ones, which enhances their ability to collect smaller particles (around 1 μm). As a result, high-efficiency cyclones are better suited for capturing fine particles, whereas high-throughput cyclones are more effective for larger particles. Additionally, cyclone efficiency is closely tied to particle size; when particle size falls below the design specifications, the efficiency of the cyclone decreases [15, 29].

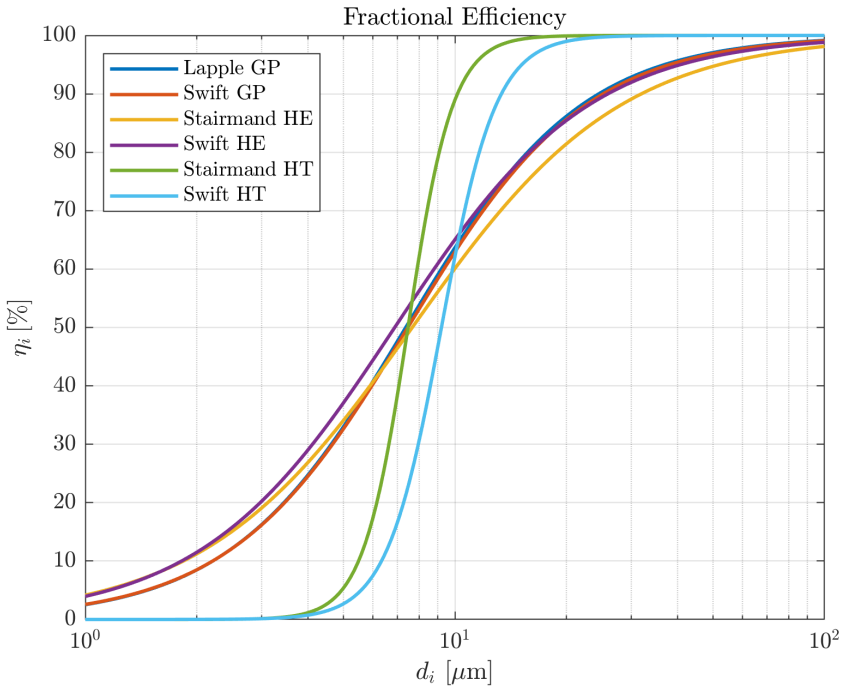

Figure 2.5: Fractional efficiency of standard cyclones for an aerosol with ρ_p=900 kg/m^3 operating at Q=10,000 m^3/h and normal conditions

2.2.4 Pressure Drop

The pressure drop in cyclones is a key operational concern, as higher values lead to increased energy costs. While improving collection efficiency often results in a greater pressure drop, a balance must be maintained between the two. Several factors contribute to pressure loss: gas expansion upon entering the cyclone chamber,

rotational kinetic energy losses, wall friction, and additional friction in the exit duct due to swirling flow. Some pressure is recovered as the rotational energy converts back into pressure energy [21, 22]. Using CFD and response surface methodology (RSM), Oranje and Janssen [30] optimized pressure drop in a Stairmand HE cyclone, identifying the vortex finder diameter as the most influential factor — smaller diameters lead to higher tangential velocities and velocity gradients, thereby increasing pressure drop. Equation 2.21 can be used to estimate the pressure drop (Δp) in the cyclone [21, 22].

$$\Delta p = \frac{\rho v^2}{2} \Delta H \tag{2.21}$$

Where ΔH is the pressure coefficient — a dimensionless parameter that depends on cyclone geometry and remains constant for geometrically similar cyclones, provided the Reynolds number (Re) is sufficiently high (i.e., in fully developed turbulent flow). Several models for ΔH have been proposed — by Shepherd and Lapple (1940), Alexander (1949), Stairmand (1949), First (1950), Barth (1956), and Casal and Benet (1983) — most of which attribute pressure losses primarily to the cyclone chamber [20, 21, 22]. Based on a statistical analysis of 98 cyclone designs, Ramachandran et al. [31] developed a more accurate predictive model for ΔH (Equation 2.22).

$$\Delta H = 20 \left(\frac{ab}{D_e^2} \right) \left[\frac{S/D}{(H/D)(h/D)(B/D)} \right]^{\frac{1}{3}} \tag{2.22}$$

Table 2.3 presents the pressure coefficient and pressure drop for the standard cyclones listed in Table 2.2, operating under the same conditions as in Figure 2.5. A clear trade-off between pressure drop and collection efficiency is observed. Among the high-efficiency cyclones, the Swift HE cyclone outperforms the Stairmand HE in efficiency but at the cost of an additional 300 Pa pressure drop. A similar trend is seen in high-throughput designs: the Stairmand HT cyclone is more efficient than the Swift HT, but the latter experiences nearly 600 Pa higher pressure drop. Overall, the pressure drop values remain close to 1000 Pa, supporting the assumption that pressure variation is relatively minor.

Parameter	**Lapple GP**	**Swift GP**	**Stairmand HE**	**Swift HE**	**Stairmand HT**	**Swift HT**	**Unit**
ΔH	6.79	6.11	4.85	7.07	7.30	6.93	-
Δp	1019	871	731	1007	1253	689	Pa

Table 2.3: Values of ΔH and Δp of standard cyclones operating at Q=10,000 m^3/h and normal conditions

2.3 Methods of Model Validation

To quantitatively assess the predictive capability of the theoretical model in reproducing the experimental collection efficiency curves, three complementary metrics were employed: the mean absolute error (MAE), the root mean square error (RMSE), and the mean testing accuracy (MTA). Together, these criteria provide a multidimensional evaluation of model performance, capturing both pointwise deviations and the overall accuracy of the predicted efficiency profiles [32, 33].

Consider $y_{obs,i}$ as the observed value of a given cyclone parameter for particle size range i, and $y_{teo,i}$ as the corresponding theoretical prediction. The MAE is defined as the average magnitude of the absolute deviations between observed and predicted values. It is mathematically defined in Equation 2.23 [32].

$$MAE = \frac{1}{n}\sum_{i=1}^{n}|y_{obs,i} - y_{teo,i}| \tag{2.23}$$

Where n is the number of particle ranges. MAE is a scale-dependent and unit-preserving metric, making it intuitively interpretable in the same physical units as the variable of interest. Because it evaluates errors in absolute terms, MAE treats all deviations equally, without disproportionately penalizing large errors. However, MAE does not distinguish between systematic and random errors and does not emphasize extreme discrepancies [32].

On the other hand, the RMSE quantifies the square root of the mean of squared deviations between observed and modeled values. In contrast to MAE, the squaring of deviations means that RMSE penalizes larger errors more severely, making it more sensitive to outliers or to model deficiencies that produce occasional large deviations. It is mathematically defined in Equation 2.24 [32].

$$RMSE = \sqrt{\frac{1}{n}\sum_{i=1}^{n}(y_{obs,i} - y_{teo,i})^2} \tag{2.24}$$

While MAE and RMSE effectively characterize local, pointwise differences between curves, they do not fully capture the global agreement between the shapes of the theoretical and experimental efficiency profiles. To address this limitation, Bregolin et al. [33] introduce the MTA as a normalized, area-based metric designed to evaluate the predictive performance of models in the context of cyclone collection efficiency. It is mathematically defined in Equation 2.25.

$$MTA = 1 - \frac{1}{n}\sum_{i=1}^{n}\frac{|y_{obs,i} - y_{teo,i}|}{|y_{obs,i}|} \tag{2.25}$$

As seen in this expression, the MTA corresponds to the complement of the mean relative absolute error, resulting in a metric bounded between 0 and 1, where values

closer to 1 indicate stronger predictive agreement. By relying on relative absolute errors, the MTA appropriately weights size classes where even small absolute deviations can represent substantial proportional differences in collection efficiency. This makes the metric particularly suitable for cyclone efficiency modeling, where the curve shape can vary substantially across the particle size spectrum [33].

Chapter 3

Materials and Methods

In this chapter, both the method and the materials for designing, manufacturing, and testing the cyclones are depicted.

3.1 Cyclone Design

As a first step, two high-efficiency cyclones (Stairmand and Swift) that work at 8 m^3/h, which is a better estimate of the actual flow rate that passes through the ISCS, were designed according to the values given in Table 2.2. The relevant dimensions achieved for both cyclones are shown in Table 3.1.

Dimension	**Stairmand HE**	**Swift HE**	**Unit**
D	38	40	mm
a	19	18	mm
b	8	8	mm
H	153	157	mm
h	57	56	mm
D_e	19	16	mm
B	14	16	mm
S	19	20	mm

Table 3.1: Relevant dimensions calculated for the designed cyclones

In addition, three other dimensions were defined: the length of the inlet (l_i), the length of the gas outlet (l_e), and the length of the particle outlet (l_h). Figure 3.1 shows where each dimension is located in the cyclone, and Table 3.2 shows the values adopted for each. Furthermore, a thickness of 2 mm was considered for this application [34, 35].

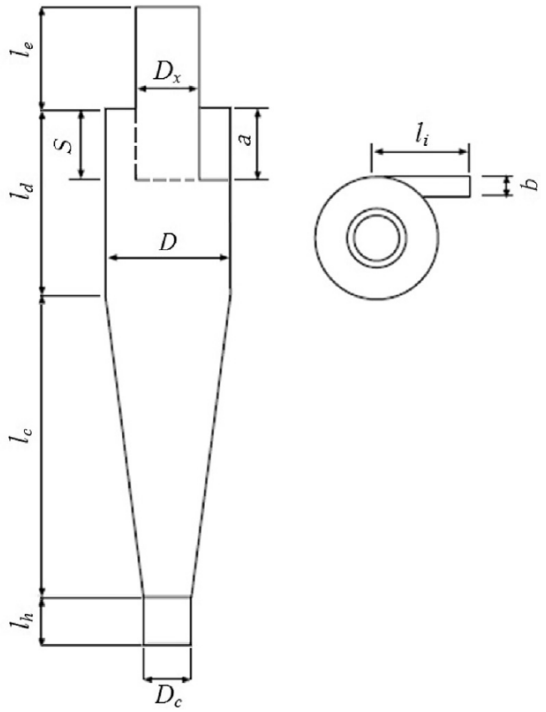

Figure 3.1: Additional dimensions of a reverse-flow cyclone with tangential inlet [34]

Dimension	Stairmand HE	Swift HE	Unit
l_i	38	40	mm
l_e	38	40	mm
l_h	15	16	mm

Table 3.2: Additional dimensions calculated for the designed cyclones

Finally, a transition between a circular section and the rectangular inlet section of the cyclone was projected to allow a connection between the device and the pipes of the experimental arrangement. In addition, a cylindrical base was added at the bottom to give better support to the cyclone. Both were drawn using SolidWorks software and manufactured using selective laser sintering (SLS) technology (Figures 3.2 and 3.3). This method uses laser irradiation to sinter thin layers of powdered material, typically polymers. Because it enables precise layering and the creation of three-dimensional objects without the use of molds or binding agents, SLS offers significant production flexibility, allowing the manufacturing of highly complex

components. The material chosen for this application was polyamide PA2200, a refined version of polyamide 12 (PA12, commonly referred to as Nylon 12). The advantageous properties of the material — namely its ability to be processed into fine powders and its strong layer adhesion during printing — play a key role in its success in this field [36].

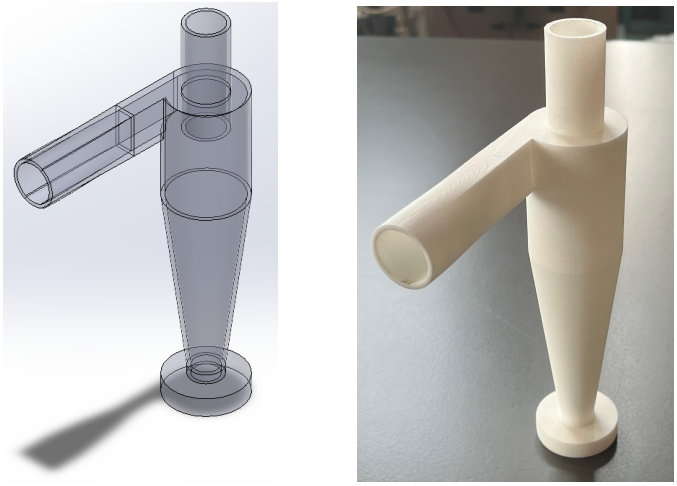

(a) On SolidWorks **(b)** Manufactured

Figure 3.2: Stairmand HE cyclone designed

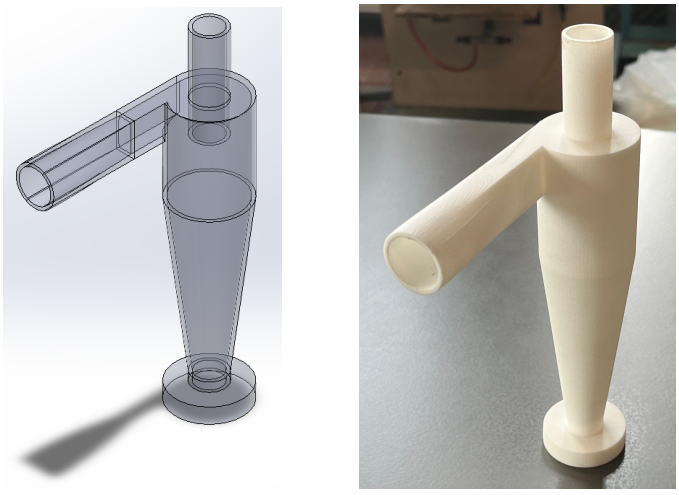

(a) On SolidWorks **(b)** Manufactured

Figure 3.3: Swift HE cyclone designed

3.2 Experimental Arrangement

Both cyclones were tested using a test rig available in the Aerosol Technology Research Lab (Figure 3.4). During the experiments, the fractional collection efficiency and pressure drop were evaluated for both devices.

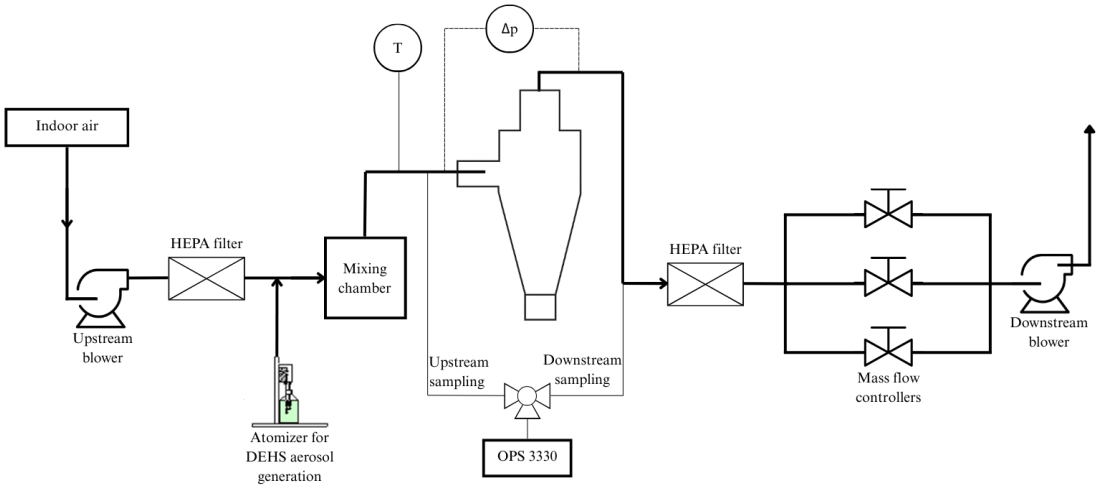

Figure 3.4: Schematic of test rig used for the experiments

The test rig features upstream and downstream blowers (Figure 3.5), with the rotational speeds of both fans electronically controlled via inverters. This configuration enables precise regulation of the airflow rate and duct overpressure by adjusting the fan speeds. Figure 3.6 shows the control panel, where one can set both volumetric flow rate and overpressure inside the system and verify the pressure drop in the cyclone [37].

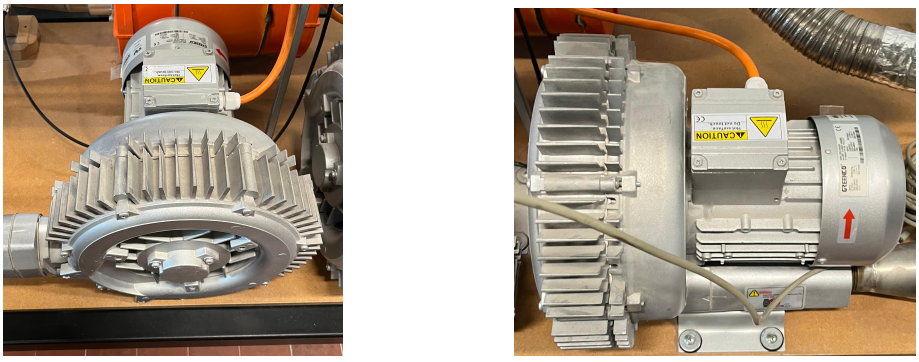

(a) Upstream blower **(b)** Downstream blower

Figure 3.5: Upstream and downstream blowers

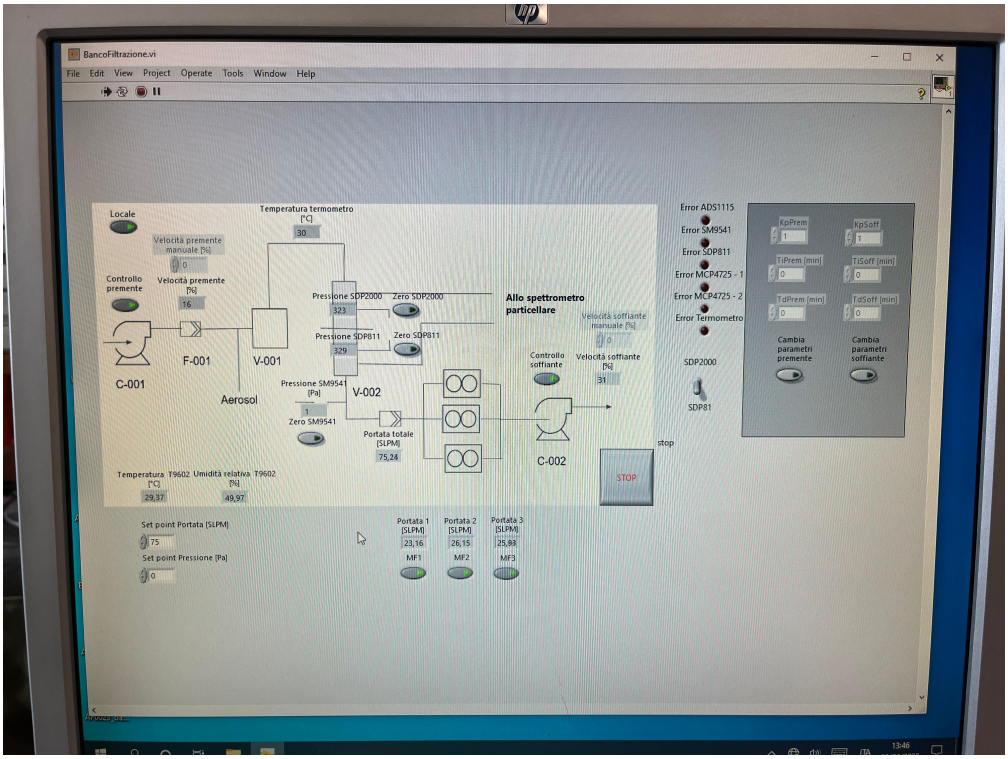

Figure 3.6: Control panel of the test rig

Air at ambient temperature and pressure enters the test rig via an upstream blower, passes through a high-efficiency particulate air (HEPA) filter to prevent particle contamination from the ambient air, and is then mixed with the test aerosol. The aerosol used in this application is di-ethyl-hexyl-sebacate (DEHS), a commonly used oil in laboratory experiments due to its low vapor pressure. Relevant properties of DEHS are summarized in Table 3.3. To generate the aerosol, compressed air feeds a Laskin nozzle submerged below the free surface of liquid DEHS contained in a reservoir, causing it to vaporize (Figure 3.7) [37, 38].

CAS number	122-62-3
Formula	$C_{26}H_{50}O_4$
Density [kg/m^3]	912
Vapour pressure (at 293 K) [Pa]	<1

Table 3.3: DEHS information and properties [39]

Figure 3.7: DEHS aerosol generator

The aerosol travels through the pipe and reaches the cyclone. An adaptation was implemented to allow the flow to exit the test rig via flexible tubing, enter the cyclone through its tangential inlet, exit it, and reenter the test rig through additional flexible tubing. At both the exit and reentry points, cones are used to direct the airflow and connect the test rig to the tubing, while a cylindrical component ensures proper sealing of the equipment (Figure 3.8). In addition, an aerosol sampling system is installed between the upstream and downstream sections of the cyclone. It consists of two sampling probes located in the upstream and downstream ducts, connected via polytetrafluoroethylene (PTFE) tubing to a three-way valve. This valve allows switching the sampling sequence between upstream sampling, downstream sampling, and clean air sampling. A schematic of this system is shown in Figure 3.9 [37].

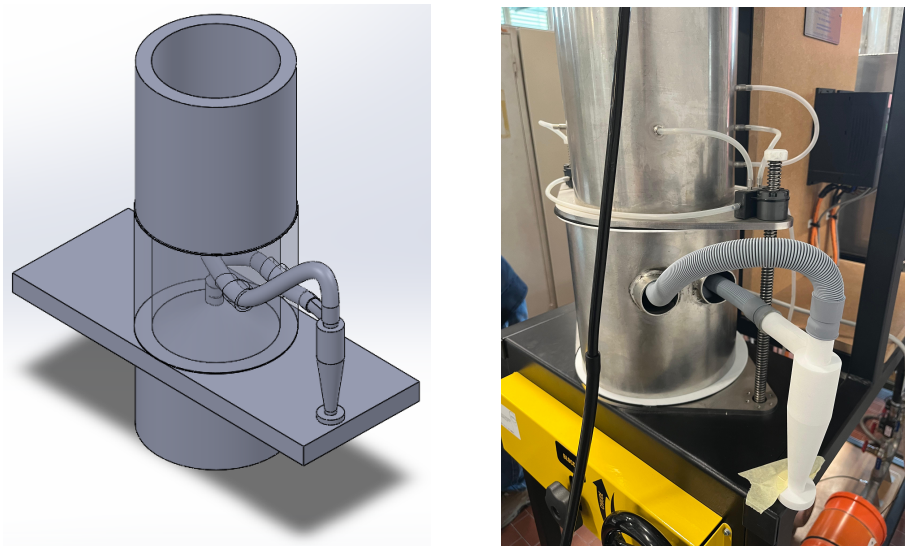

(a) On SolidWorks **(b)** Manufactured

Figure 3.8: Adaptation for the test rig

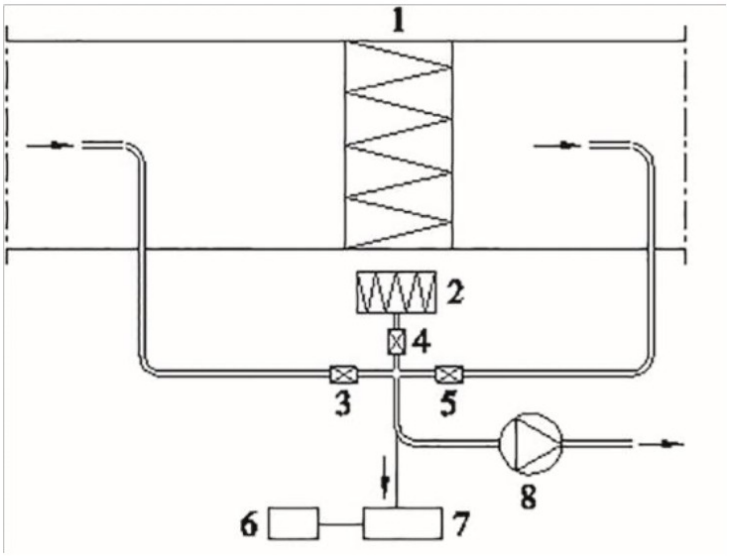

Figure 3.9: Aerosol sampling system schematic [37]

In Figure 3.9, the components are [37]:

1. Cyclone and adaptation;
2. HEPA filter used to filter intake air from the ambient;

3. Upstream sampling line valve;

4. Clean air valve;

5. Downstream sampling line valve;

6. Computer for automatic commuting and data processing;

7. Optical particle counter;

8. Auxiliary pump for suction of sampling flow.

The optical particle counter used in this application was the TSI OPS 3330, which measures particles' optical diameters in the range from 0.3 to 10 μm (Figure 3.10). It is based on the optical properties of aerosols, correlating the light intensity scattered by the particle with its size [37].

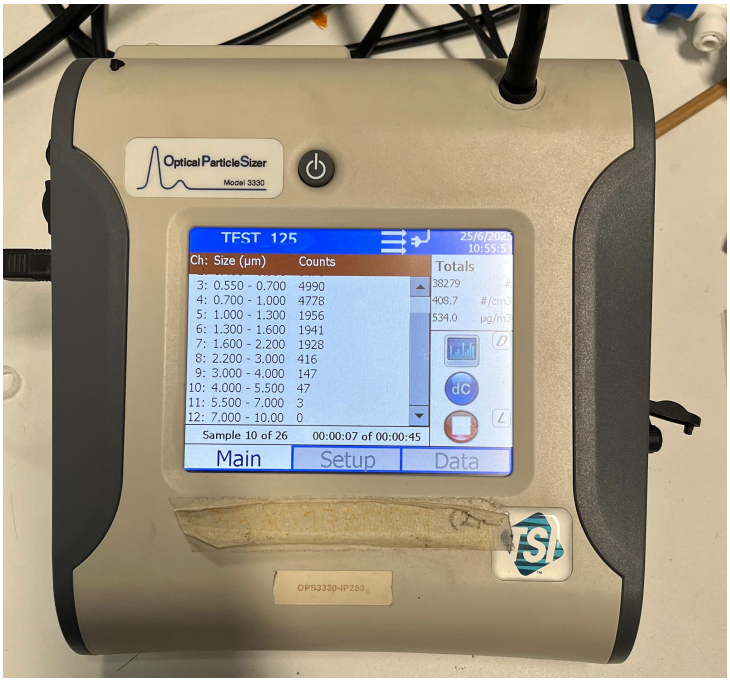

Figure 3.10: TSI OPS 3330

Finally, in the downstream pipe, in addition to the blower, there is a second HEPA filter that filters aerosol particles during tests and prevents them from exiting the test rig. Immediately after the filter, there are three manually operated valves used to regulate the airflow within the system (Figure 3.11) [37].

Figure 3.11: Three-valve scheme

3.3 Experimental Procedure

For the collection efficiency measurement, the procedure is divided into time intervals of 45 seconds each. During each interval, the optical particle counter measures the particle distribution in only one of the channels: clean air, upstream, or downstream. The first step is the zero-particle test. In this step, DEHS is not injected into the test rig, and the optical particle counter continuously monitors the particles in each channel until the number of particles detected in each channel during an interval is lower than 10 [37].

After the first step, DEHS is injected into the test rig. Once its generation stabilizes, a correlation ratio test is performed over 24 time intervals. This test evaluates the performance of the setup without the cyclone (Figure 3.12). The results from this test are later used to correct the collection efficiency measurements with the cyclone in place (Figure 3.13). This test should be conducted after any change in the flow rate [37].

Figure 3.12: Setup without the cyclone

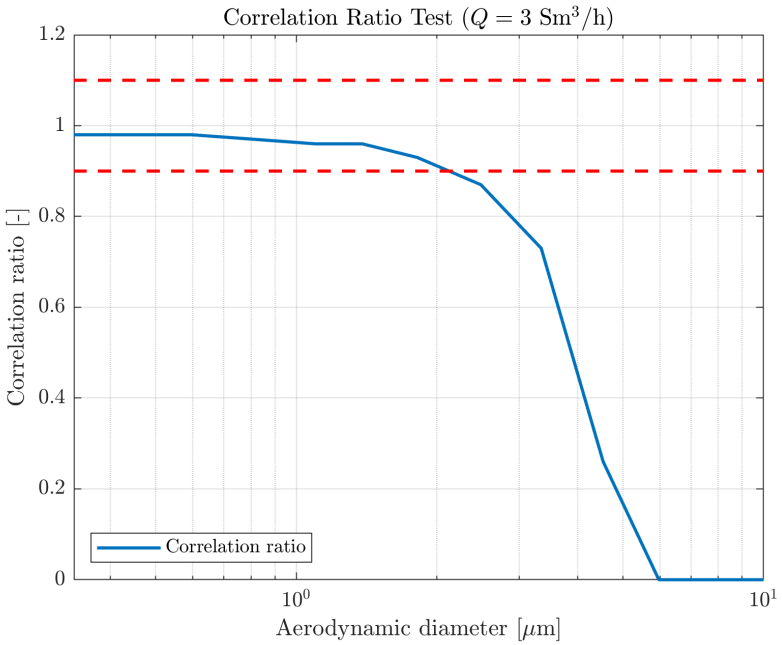

Figure 3.13: Example of results from a correlation ratio test

Finally, the collection efficiency measurement is performed. It consists of six cycles, each comprising four time intervals: one upstream, one downstream, and two purge intervals preceding each sampling phase to clean the ducts from the previous cycle. Additionally, two extra intervals are included at the end of the test, totaling 26 intervals. The partial results are calculated and monitored in real time—along with their associated uncertainties, which should ideally remain below 5% for each particle size range—using the software shown in Figure 3.14 [37].

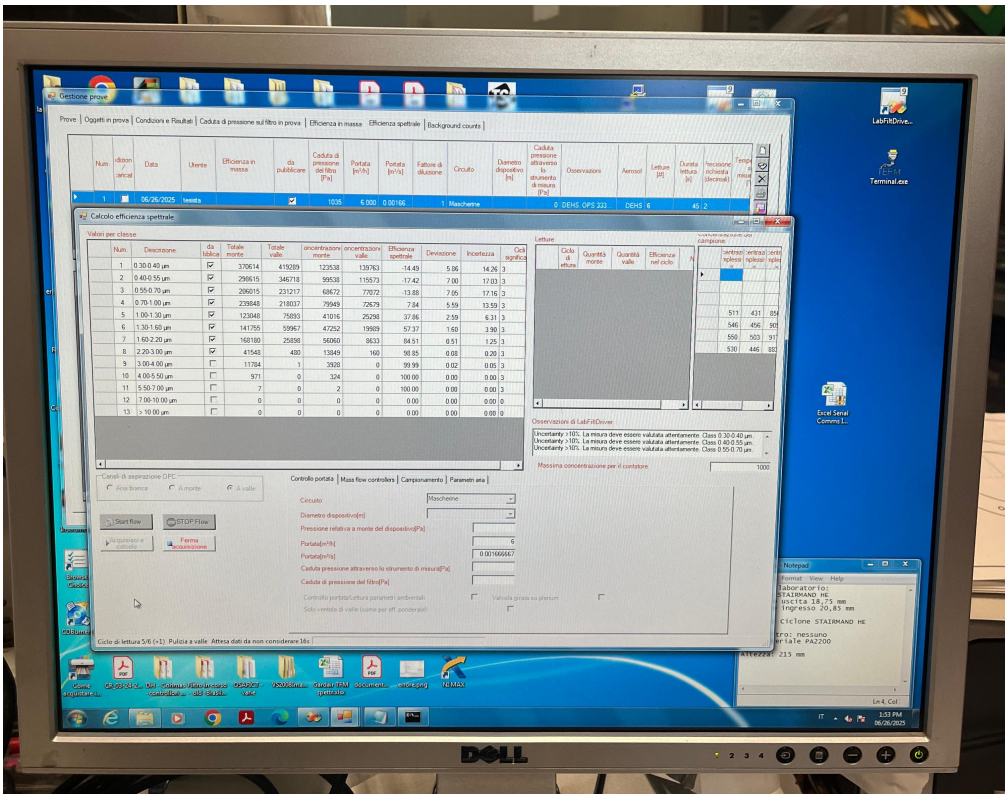

Figure 3.14: Software for collection efficiency evaluation

For the pressure drop, two different measurements were performed: one with the cyclone installed, and another with the setup without the cyclone (these measurements were carried out alongside the collection efficiency tests). The pressure drop across the cyclone is then calculated by subtracting the first value from the second.

Both measurements were performed at different volumetric flow rates. For both collection efficiency and pressure drop, five flow rates were tested — 3, 4.5, 6, 8 , and 10 m^3/h. By varying the flow rate, the inlet velocity changes, which in turn affects the cyclone's performance. However, the cyclone is designed to operate within a specific range of inlet velocities. The lower limit of this range is known

as the saltation velocity (v_s) and corresponds to the minimum value that ensures the separation between aerosol particles and gas stream. This velocity is given by Equation 3.1 [23].

$$v_s = 0.3048 \cdot 2.055 \left(\frac{W}{0.3048}\right) \left[\frac{(b/D)^{0.4}}{(1-b/D)^{\frac{1}{3}}}\right] \left(\frac{D}{0.3048}\right)^{0.067} \left(\frac{v}{0.3048}\right)^{\frac{2}{3}} \tag{3.1}$$

Where D is given in m, and W and v are given in m/s. The parameter W is calculated using Equation 3.2 [23].

$$W = \left[\frac{4\mu g(\rho_p - \rho)}{3\rho^2}\right]^{\frac{1}{3}} \tag{3.2}$$

Where g is the acceleration of gravity ($g = 9.81$ m/s^2). As for the upper limit, the American Fuel & Petrochemical Manufacturers (AFPM) recommend that cyclones should not operate at velocities exceeding 70 ft/s (approximately 21.3 m/s). According to the AFPM, such high velocities can cause wear on the internal walls of the device, ultimately compromising its performance [40].

In the tests performed, a velocity below the saltation limit was used for the 3 m^3/h case to verify whether the cyclone's collection efficiency was indeed negligible. The upper velocity limit, however, was not reached during any of the tests.

3.4 Empirical Validation of Theoretical Models

The experimental results obtained were further compared with those reported in the literature. Specifically, for collection efficiency, the Iozia and Leith model — described in Chapter 2 — was used as the theoretical reference for comparison. In addition, quantitative performance indicators were computed to assess the agreement between the experimental and theoretical efficiency curves: MAE, RMSE, and MTA, as also defined in Chapter 2. For pressure drop, the comparison was carried out using Equations 2.21 and 2.22.

To enable these comparisons, temperature and pressure data were collected during the experiments to estimate the air's density and viscosity, which are used in these models. Air density was calculated using the ideal gas law (Equation 2.3), while viscosity was estimated using Sutherland's equation (Equation 3.3) [41].

$$\mu = \mu_0 \left(\frac{T}{T_0}\right)^{\frac{3}{2}} \left(\frac{T_0 + S_S}{T + S_S}\right) \tag{3.3}$$

Where μ_0, T_0 and S_S are empirical values adjusted for each fluid. For air, their values are given in Table 3.4 [41].

Parameter	Value	Unit
μ_0	$1.716 \cdot 10^{-5}$	Pa.s
T_0	273.1	K
S_S	111	K

Table 3.4: Reference values for air in Sutherland equation [41]

The collection efficiency results were reported using the aerodynamic diameter of the particles. To achieve this, a transformation was applied to convert the measured optical diameter into the equivalent aerodynamic diameter. According to ISO/TS 19713-1, the conversion from optical diameter (D_{op}) to aerodynamic diameter (D_{ae}) can be performed using Equation 3.4 [42].

$$D_{ae} = \left(\frac{C_C(D_{op}) \cdot \rho}{C_C(D_{ae}) \cdot \rho_0 \cdot \chi} \right)^{\frac{1}{2}} \cdot D_{op} \tag{3.4}$$

Where C_C is the slip correction factor (a function of the particle diameter), ρ_0 is the unit density (1 g/cm^3 or 1000 kg/m^3), and χ is the shape factor of the test particle. This equation can be further simplified if the bulk material density is between 0.5 and 3 g/cm^3 and the particles are aerodynamically larger than 0.5 μm, as shown in Equation 3.5 [42].

$$D_{ae} = \left(\frac{\rho}{\rho_0 \cdot \chi} \right)^{\frac{1}{2}} \cdot D_{op} \tag{3.5}$$

For this application, since DEHS is a liquid aerosol, $\chi = 1$. Moreover, Equation 3.5 was applied to all measured particle sizes, including those below 0.5 μm.

Chapter 4

Results

In this chapter, the experimental results are presented, specifically those from the correlation ratio test, as well as from the collection efficiency and pressure drop measurements.

4.1 Correlation Ratio Test Results

The results of the correlation ratio tests can be seen on Figure 4.1.

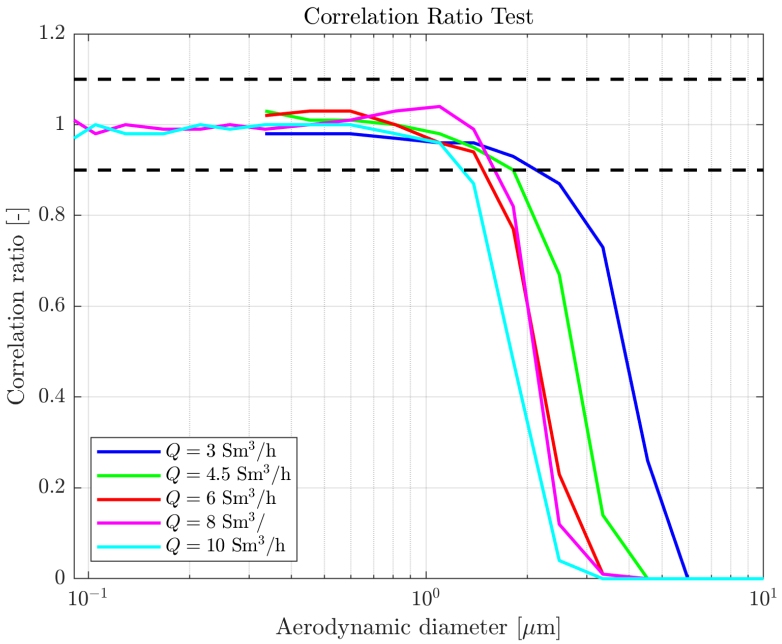

Figure 4.1: Correlation ratio test results for different values of Q

Ideally, the correlation ratio should be 1, as no particle collector is placed on the test rig. In practice, it typically ranges from 0.9 (slightly more particles detected before the adaptation) to 1.1 (slightly more particles detected after the adaptation). However, the results show that for particle sizes larger than approximately 2 μm, the correlation ratio decreases significantly, eventually approaching zero. This behavior is consistent with expectations: since the airflow exits and reenters the test rig through cones and flexible tubes that introduce curvature inside the adaptation, it is reasonable to anticipate that larger particles, due to their greater inertia, would not follow the curved path and would instead be captured by the adaptation.

4.2 Cyclone Performance Comparison

As a first step, the performance of both cyclones was compared. Figure 4.2 shows the fractional collection efficiencies obtained experimentally for both cyclones operating at 8 m^3/h, which is the design value for it.

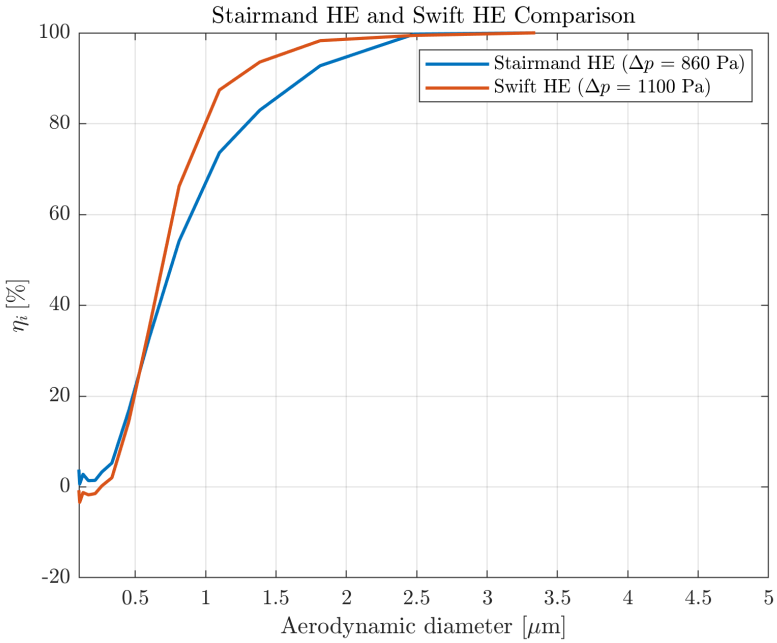

Figure 4.2: Stairmand HE and Swift HE cyclones experimental and theoretical efficiencies for Q =8 m^3/h

The comparison between the Stairmand HE and Swift HE fractional efficiency curves shows that both cyclones exhibit very similar performance across the entire particle-size range. This close agreement was expected from theoretical considerations, as both geometries are designed to achieve high efficiency in the fine-particle

regime. Nonetheless, the Swift HE demonstrates a marginally superior efficiency, particularly in the intermediate aerodynamic diameter range, where its curve rises more steeply and reaches near-complete collection slightly earlier than the Stairmand HE.

However, this modest gain in efficiency must be weighed against the substantially higher pressure drop associated with the Swift configuration relative to the Stairmand cyclone. Since pressure drop directly influences operating cost and energy consumption, the increased performance of the Swift HE does not necessarily translate into a more favorable design. Given its lower pressure drop and only slightly lower fractional efficiency, the Stairmand HE cyclone represents a better balanced and operationally suitable option for practical applications.

4.3 Model Validation

As a second step, both theoretical and experimental collection efficiencies were compared for each cyclone operating at all flow rates measured (Figures 4.3 and 4.4).

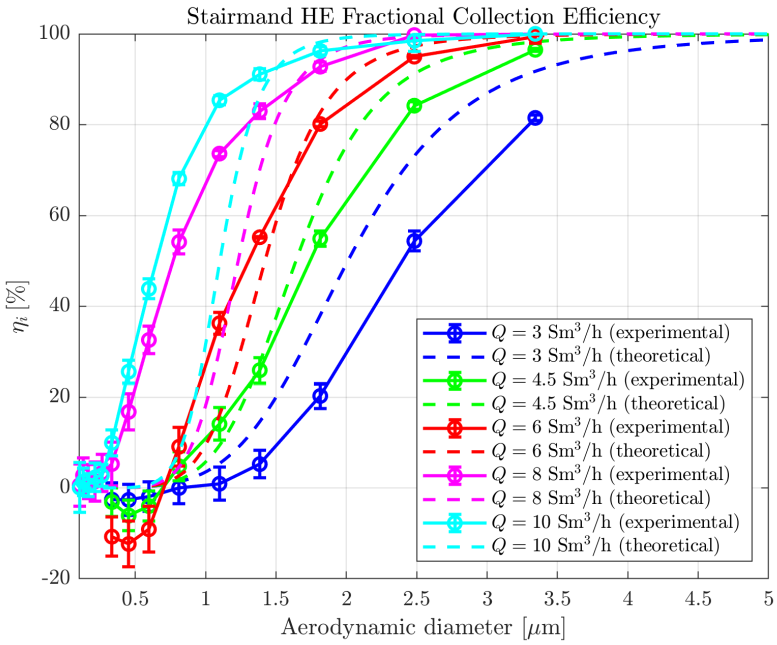

Figure 4.3: Stairmand HE cyclone experimental and theoretical efficiencies for different values of Q

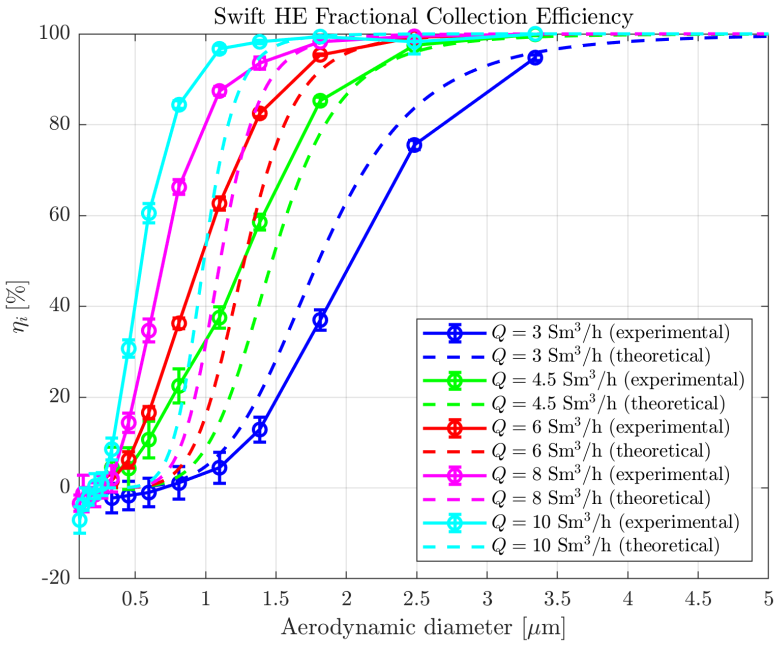

Figure 4.4: Swift HE cyclone experimental and theoretical efficiencies for different values of Q

For both cyclone geometries, the theoretical fractional efficiency curves reproduce the experimental behaviour well at moderate and high flow rates. In the Stairmand HE, predicted and observed efficiencies are closely matched at 4.5 and 6 Sm^3/h except for the three smallest size bins, where negative experimental efficiencies appear; these anomalies are consistent with amplified measurement uncertainty at low aerosol concentrations and, when error bars are considered, are not statistically significant. At the higher flow rates of 8 and 10 Sm^3/h, agreement improves further for the Stairmand: experimental and theoretical curves coincide across almost the entire size range, with only minor deviations in the smallest bins that remain within uncertainty bounds.

For the Swift HE, the experiments systematically show higher efficiencies than the model at intermediate flows (4.5–6 Sm^3/h), indicating a positive bias in measured performance relative to the semi-empirical prediction; nevertheless, at 8 and 10 Sm^3/h the experimental and theoretical curves also display close correspondence, with the experimental curves reaching high efficiencies at smaller aerodynamic diameters.

The main divergence for both cyclone geometries occurs at 3 Sm^3/h, where the model overestimates collection efficiency—particularly for the Stairmand HE. This behavior is consistent with operation below the saltation velocity, a regime in

which particle–wall separation becomes unstable and theoretical predictions lose accuracy.

A common trend observed for both cyclones is the systematic leftward shift of the fractional collection efficiency curves as flow rate increases. This reflects the expected reduction in cut-off diameter and improved capture of fine particles at higher inlet velocities, in agreement with established cyclone separation theory.

To gain deeper insight into the discrepancies between the theoretical model and the experimental results, Figures 4.5 and 4.6 depict the average uncertainty, MAE, and RMSE values for each cyclone at the respective flow rates.

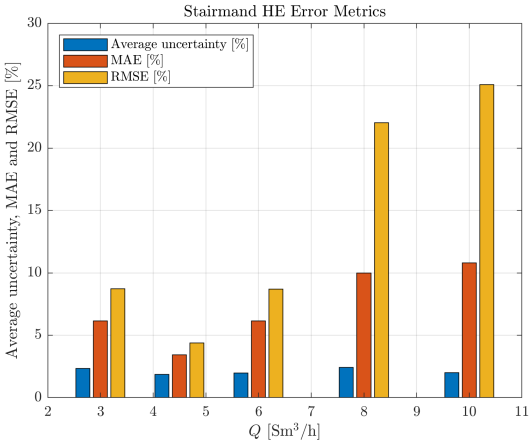

Figure 4.5: Stairmand HE cyclone error parameters

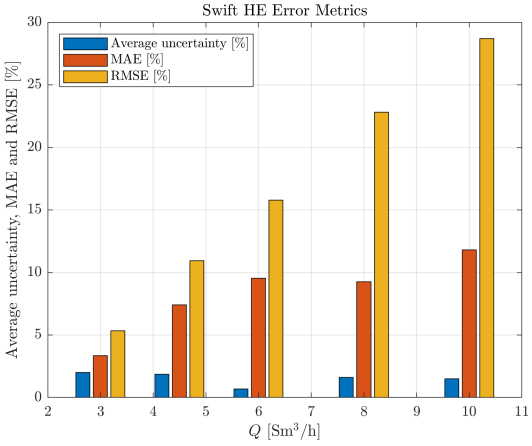

Figure 4.6: Swift HE cyclone error parameters

The analysis of the error parameters allows assessing the adequacy of the

theoretical model in relation to the experimental data obtained for the two cyclones studied. For the Stairmand HE cyclone, both MAE and RMSE increase considerably with the flow rate, particularly at 8 and 10 Sm^3/h, where RMSE values exceed 20% and 25%, respectively. At lower flow rates (3–6 Sm^3/h), the errors remain below 10% and close to the average experimental uncertainty, indicating that the theoretical model provides a consistent representation of the observed behavior. The sharp increase in error at higher flow rates suggests that, although the general curve shape is captured, local deviations become more pronounced as flow intensity and turbulence rise..

In the case of the Swift HE cyclone, the same general pattern is observed. Both MAE and RMSE gradually rise with the flow rate, reaching approximately 12% and 28% at 10 Sm^3/h, respectively. At lower flow rates, the errors are comparable to the experimental uncertainty, confirming good agreement between theoretical and experimental data. However, at higher flow conditions, the model underestimates collection efficiency, leading to larger global deviations. These results indicate that, for both cyclones, the theoretical approach performs better at low and intermediate flow rates, while its predictive accuracy decreases as the operating flow increases.

The MTA analysis, shown in Figures 4.7 and 4.8, complements these findings by providing a quantitative measure of the similarity between the experimental and theoretical efficiency curves. For the Stairmand HE cyclone, the value reaches around 90% at 4.5 and 6 Sm^3/h, confirming strong overall consistency between curves in this range. At 3 Sm^3/h, it drops to about 72%, reflecting the model's overestimation of collection efficiency at low gas velocities. Interestingly, the coefficient rises again to approximately 94% at 8 and 10 Sm^3/h, suggesting a closer match in overall curve shape. However, this apparent improvement contrasts with the higher MAE and RMSE values observed under the same conditions, indicating that the MTA may overstate the agreement by not capturing localized discrepancies in the efficiency profile. For the Swift HE cyclone, the MTA remains high and relatively uniform across the tested flow rates, ranging from 84 to 87% at lower and intermediate conditions. At 8 and 10 Sm^3/h, it increases to around 94%, suggesting an improved fit between the theoretical and experimental curves. Nevertheless, this rise also conflicts with the corresponding increase in MAE and RMSE, revealing that while the global curve shape remains similar, point-by-point deviations become more significant at higher flow rates.

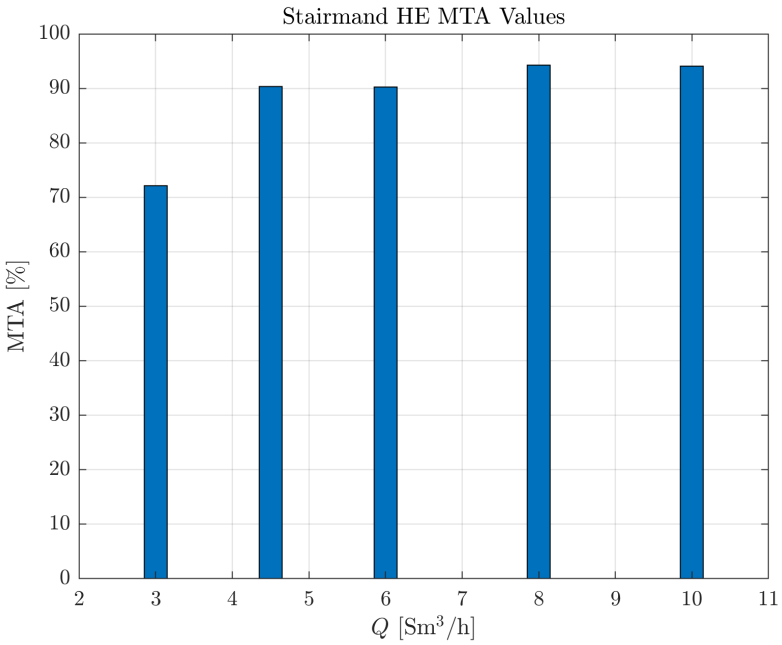

Figure 4.7: Stairmand HE cyclone MTA values

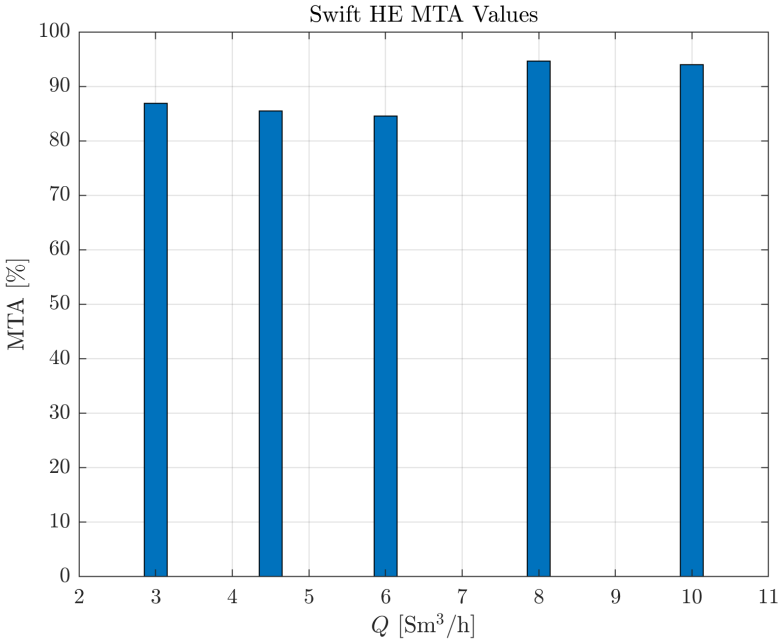

Figure 4.8: Swift HE cyclone MTA values

Overall, the combined interpretation of the error metrics and MTAs shows that both cyclones exhibit good predictive consistency at lower flow rates, with deviations close to the experimental uncertainty. At higher flow rates, despite the apparently strong overlap between theoretical and experimental curves, the growing error metrics indicate that the model's local predictive accuracy decreases. This emphasizes the importance of evaluating both global and local indicators to obtain a comprehensive understanding of model reliability under different operating conditions.

Moreover, both theoretical and experimental pressure drops were compared for each cyclone at all flow rates measured (Figures 4.9 and 4.10). The pressure drop curves obtained experimentally exhibit consistently higher values than those predicted by the theoretical model. This divergence becomes more pronounced at higher flow rates, where the experimental Δp increases at a faster rate than the theoretical trend. Such behavior suggests that additional losses—such as frictional effects, turbulence intensification, or minor geometric deviations—become increasingly relevant as the volumetric flow rate rises, leading to a steeper experimental curve. Furthermore, both sets of curves display a characteristic parabolic-like growth, which is consistent with the quadratic dependence of pressure drop on velocity (and therefore on flow rate) in cyclone separators. This parabolic behavior reflects the fundamental fluid-dynamic relationship in which inertia-dominated flow regimes cause Δp to rise disproportionately with increasing Q. The theoretical predictions capture this trend, but the experimental results amplify it due to the additional dissipative mechanisms present in real operating conditions.

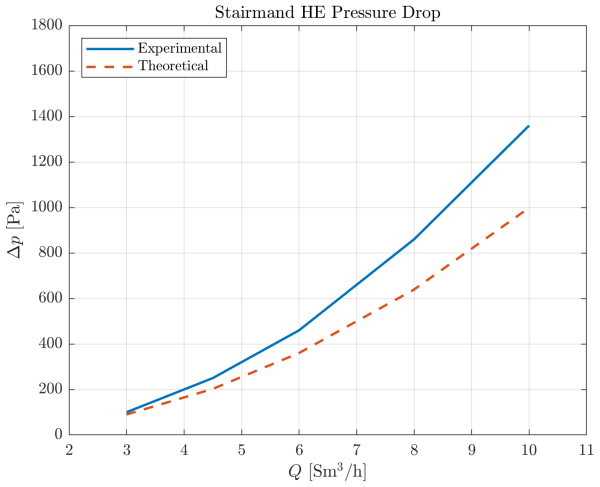

Figure 4.9: Theoretical and experimental pressure drops of a Stairmand HE cyclone for different values of Q

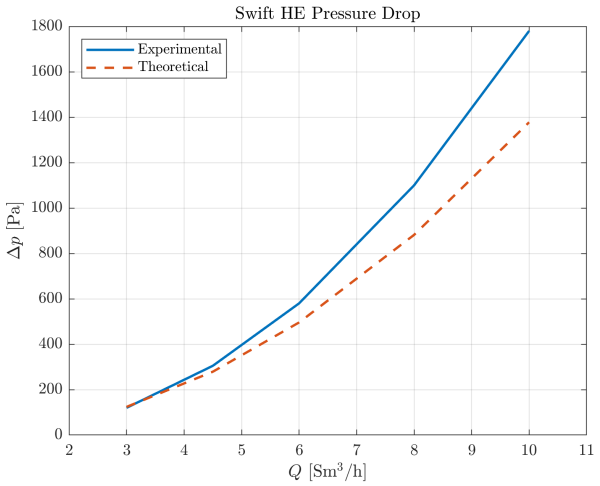

Figure 4.10: Theoretical and experimental pressure drops of a Swift HE cyclone for different values of Q

Overall, the comparison indicates that while the theoretical model successfully reproduces the qualitative (parabolic) behavior of the pressure-drop response, it systematically underestimates the magnitude of losses encountered experimentally, especially in the upper range of flow rates.

Chapter 5

Conclusion

The present work aimed to evaluate the performance of two high-efficiency cyclones — Stairmand HE and Swift HE — specifically designed to meet the operational requirements of the ISCS system. Through detailed geometric design, fabrication via selective laser sintering (SLS), and a comprehensive experimental campaign, it was possible to characterize the aerodynamic behavior of both devices and assess the predictive capability of the Iozia and Leith model under the tested conditions.

The results showed that, at low and intermediate flow rates, both cyclones exhibited fractional collection efficiency curves consistent with theoretical predictions, with deviations falling within the expected range of experimental uncertainties. As anticipated from the literature, the Swift HE consistently outperformed the Stairmand HE in terms of efficiency, though at the cost of a higher pressure drop. At higher flow rates, however, the apparent overlap between theoretical and experimental curves did not necessarily imply improved local accuracy, as reflected by increases in MAE and RMSE. This behavior highlights the importance of jointly considering global and pointwise performance indicators when evaluating the reliability of predictive models.

Regarding pressure drop, both cyclones showed experimental values systematically higher than those forecasted by theory, especially at elevated flow rates. The growing discrepancy suggests that dissipative mechanisms not captured by classical models — such as intensified turbulence, additional friction in the experimental adaptation, or small geometric inaccuracies — become increasingly relevant as the flow strengthens. Nevertheless, the characteristic parabolic trend observed in all cases confirms the dominance of inertial effects in the overall pressure-loss behavior.

Overall, the findings demonstrate that both cyclones are viable candidates to replace the separator currently used in the ISCS, offering improved predictability and potential for optimization. The Swift HE provides superior collection efficiency, while the Stairmand HE imposes a lower pressure penalty, forming a trade-off that may guide future design choices depending on system priorities.

The main limitation of this work lies in the fact that all tests were performed with DEHS aerosol in a controlled laboratory environment, which does not fully replicate the physical and chemical characteristics of the condensable vapors present in the real ISCS process. For future work, it is recommended that the performance of the cyclones be evaluated directly in the real ISCS operating environment, enabling validation under representative thermodynamic, chemical, and flow conditions, and providing a more definitive assessment of their applicability to the system.

In summary, this study provides a solid technical foundation for developing a new inertial separator for the ISCS and enhances the understanding of the interplay between experimental behavior and theoretical predictions in high-efficiency cyclone separators.

Bibliography

[1] N. Hagemann, K. Spokas, H. P. Schmidt, R. Kägi, M. A. Böhler, and T. D. Bucheli. «Activated Carbon, Biochar and Charcoal: Linkages and Synergies across Pyrogenic Carbon's ABCs». In: *Water* 10(2) (Feb. 2018) (cit. on p. 1).

[2] J. A. Olivares, D. Puyol, J. A. Melero, and J. Dufour. *Wastewater Treatment Residues as Resources for Biorefinery Products and Biofuels*. First Edition. Elsevier, 2019. Chap. 8 (cit. on pp. 1, 4).

[3] R. Phiri, S. M. Rangappa, and S. Siengchin. «Agro-waste for renewable and sustainable green production: A review». In: *Journal of Cleaner Production* 434 (Jan. 2024) (cit. on p. 1).

[4] M. L. Schmid, A. C. Barros, F. Costa, and L. C. T. Rieth. «CARVÃO VEGETAL NO BRASIL: UMA VISÃO PANORÂMICA DO MERCADO E SUAS PERSPECTIVAS». In: *Boletim Técnico SIF* 4(5) (May 2024) (cit. on pp. 1, 4).

[5] P. L. Froehlich and A. Moura. «CARVÃO VEGETAL: PROPRIEDADES FÍSICO-QUÍMICAS E PRINCIPAIS APLICAÇÕES». In: *Revista Tecnologia e Tendências* 9(1) (2014) (cit. on p. 1).

[6] A. M. M. Santi and Z. L. Gonçalves. «Behind the smoke screen: working and living in brazilian charcoal production farms». In: *Revista Tecnologia e Sociedade* 15(37) (2019), pp. 429–444 (cit. on pp. 1–4).

[7] A. Al-Rumaihi, M. Shahbaz, G. Mckay, H. Mackey, and T. Al-Ansari. «A review of pyrolysis technologies and feedstock: A blending approach for plastic and biomass towards optimum biochar yield». In: *Renewable and Sustainable Energy Reviews* 167 (Oct. 2022) (cit. on p. 3).

[8] S. F. O. M. Santos and K. Hatakeyama. «Sustainable charcoal production process focusing the environmental, economical, social and cultural aspects». In: *Produção* 22(2) (2012), pp. 309–321 (cit. on p. 3).

[9] World Steel Association. «Sustainability performance of the steel industry 2003-2023». In: (Nov. 2024) (cit. on p. 4).

[10] International Energy Association (IEA). «Tracking Clean Energy Progress 2023». In: (July 2023) (cit. on p. 4).

[11] H. Muslemani, X. Liang, K. Kaesehage, F. Ascui, and J. Wilson. «Opportunities and challenges for decarbonizing steel production by creating markets for 'green steel' products». In: *Journal of Cleaner Production* 315 (Sept. 2021) (cit. on p. 4).

[12] R. Atkinson and J. Arey. «Atmospheric Degradation of Volatile Organic Compounds». In: *Chemical Reviews* 103 (Oct. 2003), pp. 4605–4638 (cit. on p. 4).

[13] S. H. Hong, D. C. Shin, Y. J. Lee, S. H. Kim, and Y. W. Lim. «Health risk assessment of volatile organic compounds in urban areas». In: *Human and Ecological Risk Assessment: An International Journal* 23(6) (July 2017), pp. 1454–1465 (cit. on p. 4).

[14] J. Vallejo, M. Dalmasso, M. J. Rubio, J. Marval, V. Gentile, and P. Tronville. «SEPARATION OF AEROSOLS INDUCING LOCALIZED CONDENSATION OF VAPORS». In: *FILTECH 2023*. Cologne, Germany, Feb. 2023 (cit. on pp. 4–7).

[15] B. G. Miller. *Clean Coal Engineering Technology*. Second Edition. Elsevier, 2017. Chap. 8 (cit. on pp. 10, 11, 13–15, 17–20).

[16] A. J. Macintyre. *Ventilação Industrial e Controle da Poluição*. Second Edition. Editora Guanabara, 1990 (cit. on p. 10).

[17] C. A. Clezar and A. C. R. Nogueira. *Ventilação Industrial*. Florianópolis: Editora da UFSC, 1999 (cit. on pp. 10, 12, 13).

[18] E. E. S. Lora. *Prevenção e Controle de Poluição nos Setores Energético, Industrial e de Transporte*. Second Edition. Rio de Janeiro: Editora Interciência, 2002 (cit. on pp. 11–13).

[19] W. C. Hinds. *Aerosol Technology - Properties, Behavior, and Measurement of Airborne Particles*. Second Edition. John Wiley & Sons, Inc., 1999 (cit. on pp. 13–15, 18).

[20] A. C. Hoffmann and L. E. Stein. *Gas Cyclones and Swirl Tubes - Principles, Design and Operation*. Second Edition. Springer, 2010 (cit. on pp. 13, 14, 16, 18, 21).

[21] L. K. Wang, N. C. Pereira, and Y. Hung. *Air Pollution Control Engineering*. Volume 1. Humana Press Inc., 2004. Chap. 3 (cit. on pp. 13, 15–19, 21).

[22] D. Leith and D. Mehta. «CYCLONE PERFORMANCE AND DESIGN». In: *Atmospheric Environment* 7 (May 1973), pp. 527–549 (cit. on pp. 16–18, 21).

[23] A. C. O. De Paula, J. R. Henríquez, and F. A. B. Figueiredo. «VALIDATION OF A PROCEDURE FOR DIMENSIONING A CYCLONE SEPARATOR FOR CIRCULATING FLUIDIZED BED GASIFIER». In: *13th International Conference on Heat Transfer, Fluid Mechanics and Thermodynamics*. Portorož, Slovenia, July 2017 (cit. on pp. 17, 35).

[24] H. Yang, N. Wang, Y. Cao, X. Meng, and L. Yao. «Effects of helical fins on the performance of a cyclone separator: A numerical study». In: *Advanced Powder Technology* 34 (Jan. 2023) (cit. on p. 18).

[25] N. Sylvia, H. Husin, A. Muslim, Yunardi, A. Syahrullah, H. Purnomo, R. Dewi, and Y. Bindar. «Design and performance of a cyclone separator integrated with a bottom ash bed for the removal of fine particulate matter in a palm oil mill: A simulation study». In: *AIMS Environmental Science* 10 (Apr. 2023), pp. 341–355 (cit. on p. 18).

[26] B. Zhao. «Development of a Dimensionless Logistic Model for Predicting Cyclone Separation Efficiency». In: *Aerosol Science and Technology* 44 (2010), pp. 1105–1112 (cit. on pp. 18, 19).

[27] J. Dirgo and D. Leith. «Cyclone Collection Efficiency: Comparison of Experimental Results with Theoretical Predictions». In: *Aerosol Science and Technology* 4 (1985), pp. 401–415 (cit. on p. 18).

[28] D. L. Iozia and D. Leith. «Effect of Cyclone Dimensions on Gas Flow Pattern and Collection Efficiency». In: *Aerosol Science and Technology* 10 (1989), pp. 491–500 (cit. on p. 19).

[29] D. L. Iozia and D. Leith. «The Logistic Function and Cyclone Fractional Efficiency». In: *Aerosol Science and Technology* 12 (1990), pp. 598–606 (cit. on pp. 19, 20).

[30] J. Oranje and J. Janssen. «OPTIMISATION OF STAIRMAND'S CYCLONE SEPARATOR FOR REDUCED ENERGY CONSUMPTION». In: *FILTECH 2024*. Cologne, Germany, Nov. 2024 (cit. on p. 21).

[31] G. Ramachandran, D. Leith, J. Dirgo, and H. Feldman. «Cyclone Optimization Based on a New Empirical Model for Pressure Drop». In: *Aerosol Science and Technology* 15 (1991), pp. 135–148 (cit. on p. 21).

[32] KS. Cheng, YT. Lien, YC. Wu, and YF. Su. «On the criteria of model performance evaluation for real- time flood forecasting». In: *Stoch Environ Res Risk Assess* 31 (2017), pp. 1123–1146 (cit. on p. 22).

[33] E. Bregolin, P. Danieli, and M. Masi. «Collection Efficiency of Cyclone Separators: Comparison between New Machine Learning-Based Models and Semi-Empirical Approaches». In: *Waste* 2(3) (2024), pp. 240–257 (cit. on pp. 22, 23).

[34] O. Hamdy, M. A. Bassily, H. M. El-Batshc, and T. A. Mekhail. «Numerical study of the effect of changing the cyclone cone length on the gas flow field». In: *Applied Mathematical Modelling* 46 (Jan. 2017), pp. 81–97 (cit. on pp. 24, 25).

[35] JACOB Pipework Systems. *Cyclones*. URL: https://www.jacob-group.com/products/silencers-%20cyclones/cyclones/ (cit. on p. 24).

[36] I. Malashin, D. Martysyuk, V. Tynchenko, V. Nelyub, A. Borodulin, and A. Galinovsky. «Mechanical Testing of Selective-Laser-Sintered Polyamide PA2200 Details: Analysis of Tensile Properties via Finite Element Method and Machine Learning Approaches». In: *Polymers* 16 (2024), p. 737 (cit. on p. 26).

[37] Y. Xiao. «Filtration performance of innovative fibrous media». MA thesis. Turin: Politecnico di Torino, 2024 (cit. on pp. 27–32, 34).

[38] M. Heim, B. J. Mullins, H. Umhauer, and G. Kasper. «Performance evaluation of three optical particle counters with an efficient "multimodal" calibration method». In: *Journal of Aerosol Science* 39 (Dec. 2008), pp. 1019–1031 (cit. on p. 28).

[39] *Di-Ethyl-Hexyl-Sebacate (DEHS)*. Dresden, Germany: Topas GmbH (cit. on p. 28).

[40] American Fuel & Petrochemical Manufacturers (AFPM). *Question 93: How do you manage regenerator cyclone life to ensure that you reach target turnaround intervals? Do you consider superficial velocity, inlet velocity, inlet loading, outlet velocity, etc.?* 2012. URL: https://www.afpm.org/data-reports/technical-papers/qa-%20search/question-93-how-do-you-manage-regenerator-cyclone-life#:~:text=KBR%20recommends%20that%20Operations%20maintain,an%20increase%20in%20cyclone%20efficiency. (cit. on p. 35).

[41] F. M. White. *Fluid Mechanics*. Eighth Edition. McGraw-Hill Education, 2016 (cit. on pp. 35, 36).

[42] *Road vehicles - Inlet air cleaning equipment for internal combustion engines and compressors - Part 1: Fractional efficiency testing with fine particles (0,3 µm to 5 µm optical diameter)*. ISO/TS 19713-1, 2010 (cit. on p. 36).